nature electronics

Article

https://doi.org/10.1038/s41928-024-01265-2

High-performance p-type field-effect transistors using substitutional doping and thickness control of two-dimensional materials

Received: 6 March 2024

Accepted: 24 September 2024

Published online: 06 November 2024

Check for updates

Mayukh Das[1,8], Dipanjan Sen[1,8], Najam U Sakib[1], Harikrishnan Ravichandran[1], Yongwen Sun[1], Zhiyu Zhang[1], Subir Ghosh[1], Pranavram Venkatram[1], Shiva Subbulakshmi Radhakrishnan[1], Alexander Sredenschek[2], Zhuohang Yu[2], Kalyan Jyoti Sarkar[3], Muhtasim Ul Karim Sadaf[1], Kalaiarasan Meganathan[3], Andrew Pannone[1], Ying Han[1], David Emanuel Sanchez[2], Divya Somvanshi[4], Zdenek Sofer[3], Mauricio Terrones[2,5], Yang Yang[1,6,7] & Saptarshi Das[1,5,7]

In silicon field-effect transistors (FETs), degenerate doping of the channel beneath the source and drain regions is used to create high-performance n- and p-type devices by reducing the contact resistance. Two-dimensional semiconductors have, in contrast, relied on metal-work-function engineering. This approach has led to the development of effective n-type 2D FETs due to the Fermi-level pinning occurring near the conduction band, but it is challenging with p-type FETs. Here we show that the degenerate p-type doping of molybdenum diselenide and tungsten diselenide—achieved through substitutional doping with vanadium, niobium and tantalum—can reduce the contact resistance to as low as 95 Ω μm in multilayers. This, though, comes at the cost of poor electrostatic control, and we find that the doping effectiveness—and its impact on electrostatic control—is reduced in thinner layers due to strong quantum confinement effects. We, therefore, develop a high-performance p-type 2D molybdenum diselenide FET using a layer-by-layer thinning method to create a device with thin layers at the channel and thick doped layers at the contact regions.

Two-dimensional (2D) semiconductors have emerged as a potential alternative to silicon in complementary metal–oxide–semiconductor technology[1–3]. Transition metal dichalcogenides (TMDs)—such as molybdenum disulfide (MoS_2), molybdenum diselenide ($MoSe_2$) and tungsten diselenide (WSe_2)—can be as thin as around 0.6 nm at the monolayer limit and yet offer atomically smooth and dangling-bond-free surfaces that are difficult to achieve in bulk semiconductors at similar thicknesses[1–3]. Developments in n-type field-effect transistors (FETs) based on 2D materials like MoS_2 and WS_2 have brought them closer to meeting the International Roadmap for Devices and Systems requirements[4–7]. These developments include advances in high-quality material growth[8,9], contact engineering[10,11], aggressive channel-length scaling[11,12] and high-κ dielectric integration[13,14]. However, progress with p-type 2D FETs has been much slower.

The absence of p-type transport in 2D TMDs is attributed to Fermi-level pinning at the metal–2D contact interfaces[15]. In the case of transition metal (TM) sulfides like MoS_2 and WS_2, pinning occurs near the conduction band edge (E_C) (ref. 16 and Supplementary

A full list of affiliations appears at the end of the paper. e-mail: sud70@psu.edu

Fig. 1a). In n-type FETs, high performance can be achieved by using low-work-function metals (such as scandium, bismuth and antimony) as the contact electrodes to create a near-zero Schottky barrier (SB) height for electron injection ($\phi_{SB\text{-}N}$) (refs. 10,16). However, this inherently causes a large SB height for hole injection ($\phi_{SB\text{-}P} = E_G - \phi_{SB\text{-}N}$, where E_G is the TMD bandgap) that remains unaffected even when high-work-function metals (such as nickel (Ni), palladium (Pd) or platinum (Pt)) are used, thereby contributing to a high contact resistance (R_C). This is further exacerbated in monolayers of metal sulfides because they have larger bandgap values compared with their multilayer counterparts, explaining the absence of reported p-type FETs based on monolayer MoS_2 and WS_2.

In TM selenides like $MoSe_2$ and WSe_2, Fermi-level pinning occurs near the middle of the bandgap[17], facilitating relatively easier hole injection (Supplementary Fig. 1b). However, due to the prevalence of tunnelling injection across the SB as opposed to thermionic emission over the SB, $MoSe_2$ and WSe_2 FETs exhibit diminished ON-state performance (I_{ON}) (ref. 18). To achieve a high-performance p-type 2D FET, the R_C value must be reduced either by reducing the SB height for holes or reducing the SB tunnelling distance, which is the width of the depletion region at the metal–semiconductor interface (W_{SB}). This is determined by the semiconductor doping (N_D) as

$$W_{SB} \approx \sqrt{2\varepsilon_{body}\phi_{SB\text{-}P}/qN_D}, \quad (1)$$

where ε_{body} is the permittivity of the semiconducting channel and q is the elementary charge. The semiconductor industry has typically reduced R_C for n- and p-type FETs through the degenerate doping of silicon underneath the contacts since Fermi-level pinning also occurs at metal–silicide junctions[19]. The channel, however, is kept intrinsic or non-degenerately doped based on the threshold voltage requirements of the circuit designers. Therefore, a selected area with substitutional doping plays a critical role in enabling high-performance silicon FETs.

In this Article, we show that the substitutional doping of $MoSe_2$ and WSe_2 single crystals can be used to create p-type FETs with low R_C. Although pristine flakes exhibit dominant n-type transport irrespective of flake thickness, FETs based on thick flakes (around 4–6 layers) of 2D crystals doped with vanadium (V), niobium (Nb) and tantalum (Ta) exhibit degenerate p-type doping. These FETs offer an I_{ON} value as high as ~1.8 mA μm^{-1}, better channel-length scaling and R_C as low as ~95 Ω μm. However, they also have poor electrostatic gate control, resulting in a low ON/OFF current ratio (<20). As the thickness of the flake decreases, the effectiveness of doping diminishes due to quantum confinement effects (QCE), which can be explained using density functional theory (DFT) calculations[20,21]. FETs based on thin flakes (~1–3 layers) are found to have a relatively higher ON/OFF current ratio (>10^5) but high R_C (>25 kΩ μm) and thus limited I_{ON} (<10 μA μm^{-1}).

These findings highlight the importance of using degenerate doping to decrease R_C and emphasize the need to maintain a thin channel for improved electrostatics. This led us to design an FET structure in which the channel consists of 1–3 layers of 2D material, whereas the contact regions comprise degenerately doped multilayers (>6 layers), allowing us to achieve both high I_{ON} (~85 μA μm^{-1}; due to low $R_C \approx 2$ kΩ μm) and high ON/OFF current ratio of >10^4 in a back-gated device. We also show that a scaled dual-gated FET with channel length $L_{CH} = 50$ nm demonstrates even higher $I_{ON} \approx 212$ μA μm^{-1} owing to better electrostatic control of the channel region. To create this structure, a controlled layer-by-layer thinning method is used to reduce the thickness of the channel region to a single layer and protecting the multilayer regions underneath the contacts. Our design approach could be expanded to a range of 2D materials, including both n- and p-type doping. It could also be extended to large-area synthetic 2D materials.

Layer-thickness-dependent doping efficacy in 2D materials

We first prepared pristine and doped $MoSe_2$ and WSe_2 single crystals using a chemical vapour transport (CVT) technique, introducing dopants such as V, Nb and T, which belong to group VB and have different atomic radii. These dopants were selected based on prior DFT calculations, aiming to discover appropriate TM dopants capable of inducing p-type doping in single-layer WSe_2 (ref. 22). After the crystals were synthesized, inductively coupled plasma atomic emission spectroscopy (ICP-AES) was used to determine the bulk doping concentrations for various dopants for $MoSe_2$ and WSe_2 (Extended Data Fig. 1a,b, respectively). To confirm that the bulk doping concentration translates to micrometre-scale flakes, energy-dispersive X-ray spectroscopy (EDS) measurements were also performed using scanning electron microscopy (SEM) for various dopants and the results are summarized in Extended Data Fig. 1c,d for $MoSe_2$ and WSe_2, respectively. The results from ICP-AES and SEM-EDS were found to be similar. The concentrations of V, Nb and Ta were found to be less than 0.8 at.% and 0.4 at.% for $MoSe_2$ and WSe_2, respectively. Furthermore, for both materials, the doping concentration for Ta was found to be the highest, whereas V doping was the lowest.

Although ICP-AES and SEM-EDS results validate the presence of incorporated dopants in the crystals, they do not establish whether the introduced dopant atoms attain electrical activation and contribute to the intended electronic properties of the semiconductor material. To address this, Hall measurements were conducted to determine the carrier concentration and type. Extended Data Fig. 1e,f shows the room-temperature bulk carrier concentrations (N_B) obtained from Hall measurements for V-, Nb- and Ta-doped $MoSe_2$ and WSe_2, respectively. For all the dopant variations in both materials, the carrier concentrations were consistently identified as p type. For $MoSe_2$, the N_B values were found to be 1.51×10^{19} cm^{-3}, 1.57×10^{19} cm^{-3} and 5.36×10^{19} cm^{-3} for V-, Nb- and Ta-doped crystals, which corresponds to active dopant concentrations of ~0.08 at.%, ~0.085 at.% and ~0.285 at.%, respectively. For WSe_2, the N_B values were found to be 1.74×10^{19} cm^{-3}, 2.13×10^{19} cm^{-3} and 1.91×10^{19} cm^{-3} for V-, Nb- and Ta-doped crystals, which corresponds to active dopant concentrations of ~0.115 at.%, ~0.14 at.% and ~0.125 at.%, respectively. These results confirm the partial electrical activation of the respective dopant atoms in the corresponding bulk crystals.

Next, FETs were fabricated using exfoliated flakes from these crystals on a Si substrate with a global back-gate stack of 50-nm-thick alumina (Al_2O_3), grown via atomic layer deposition (ALD), on top of electron-beam (e-beam)-evaporated Ti/Pt. To define the source and drain contacts, e-beam lithography was used, followed by e-beam evaporation of 40/30 nm Pd/Au as the contact metal. Pd was chosen due to its high work function, which facilitates more efficient hole injection. Extended Data Fig. 2a,b shows the transfer characteristics, that is, source-to-drain current (I_{DS}) as a function of the back-gate voltage (V_{BG}) for a constant source-to-drain bias of $V_{DS} = 1$ V for representative thick (~4–6 monolayers) and thin (~1–3 monolayers) pristine $MoSe_2$ FETs. Extended Data Fig. 2c,d shows similar results for pristine thick and thin WSe_2 FETs, respectively. All the FETs have L_{CH} of 500 nm. Note that it is difficult to confirm whether the n-type doping observed in FETs based on pristine $MoSe_2$ and WSe_2 is due to impurities present in the as-grown materials or from the substrate. We note that the substrate used for our device fabrication, that is, ALD-grown Al_2O_3, is known to introduce n-type doping in 2D semiconductors[23]. Furthermore, metal Fermi-level pinning can also influence the observed n-type transport. According to our experimental results, both TMDs display dominant n-type transport behaviour with comparatively weaker hole branches. This observation indicates that the metal Fermi level is pinned closer to the middle of the bandgap, exhibiting greater proximity to the conduction band rather than the valence band.

Figure 1a–f shows the transfer characteristics for several thick (~4–6 monolayers) and thin (~1–3 monolayers) V-, Nb- and Ta-doped $MoSe_2$ FETs. Extended Data Fig. 3a–f shows similar results for V-,

https://doi.org/10.1038/s41928-024-01265-2

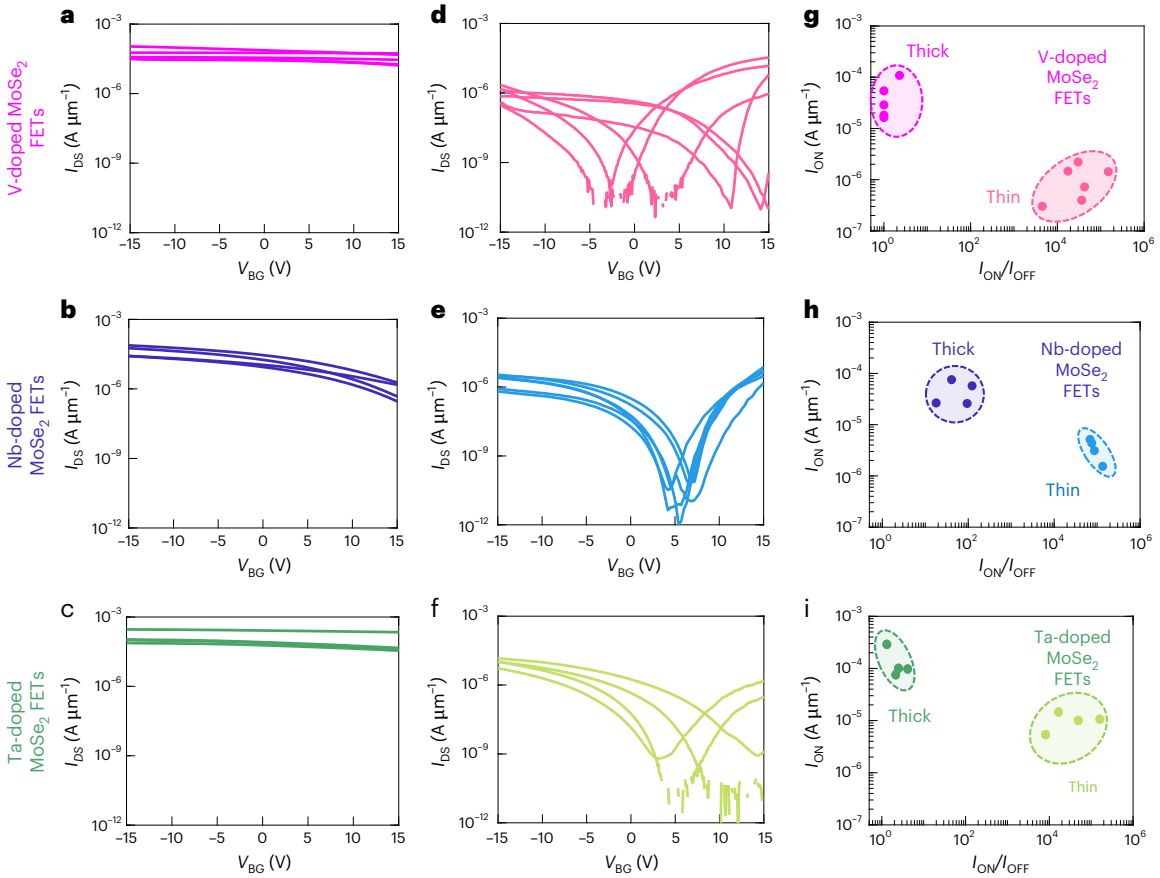

Fig. 1 | Substitutionally doped p-type $MoSe_2$ FETs. a–c, Transfer characteristics, that is, source-to-drain current (I_{DS}) as a function of V_{BG} for a constant source-to-drain bias of V_{DS} = 1 V for V-doped (**a**), Nb-doped (**b**) and Ta-doped (**c**) $MoSe_2$ FETs with thick (~4–6 monolayers) channels. These FETs show high ON-state current (I_{ON}) and poor electrostatic gate control (low I_{ON}/I_{OFF}), confirming degenerate p-type doping. **d–f**, Transfer characteristics for V-doped (**d**), Nb-doped (**e**) and Ta-doped (**f**) $MoSe_2$ FETs with thin (~1–3 monolayers) channels, retaining high I_{ON}/I_{OFF} values of more than 10^5. However, the I_{ON} values were much lower. **g–i**, Corresponding scatter plots with I_{ON} measured at V_{BG} = −15 V and I_{ON}/I_{OFF} as the two axes for V-doped (**g**), Nb-doped (**h**) and Ta-doped (**i**) FETs with thick and thin $MoSe_2$ channels. All FETs have L_{CH} of 500 nm.

Nb- and Ta-doped thick and thin WSe_2 FETs, respectively. All the FETs have L_{CH} of 500 nm. Although degenerate p-type doping is seen in FETs with thick channels for both materials irrespective of the dopant type, none of the FETs based on thick flakes could be turned OFF using the V_{BG} range of −15 V to 15 V, resulting in poor current ON/OFF ratios (I_{ON}/I_{OFF}). In contrast, the FETs based on thin channels were found to be non-degenerately doped irrespective of the dopant type for both $MoSe_2$ and WSe_2, enabling the retention of electrostatic gate control and resulting in an I_{ON}/I_{OFF} exceeding 10^5. Although these thin FETs show ambipolar transfer characteristics, it is reasonable to assert that the incorporation of V, Nb and Ta dopants resulted in p-type doping, even in thinner flakes. This is supported by the fact that the intrinsic materials exclusively exhibited n-type unipolar transport. As we will elucidate later using DFT calculations, ambipolar transport is also facilitated due to bandgap narrowing in doped $MoSe_2$. Figure 1g–i and Extended Data Fig. 3g–i show the scatter plots for these V, Nb- and Ta-doped FETs with thick and thin $MoSe_2$ and WSe_2 channels with I_{ON} values measured at V_{BG} = −15 V using V_{DS} = 1 V and I_{ON}/I_{OFF} as the two axes. The $MoSe_2$ FETs with thicker channels demonstrate median I_{ON} values of ~38 μA μm^{-1}, ~45 μA μm^{-1} and ~100 μA μm^{-1} for V, Nb and Ta dopants, respectively, whereas the median I_{ON} values dropped to 1.4 μA μm^{-1}, ~2.5 μA μm^{-1} and ~10 μA μm^{-1} for the same dopant type for $MoSe_2$ FETs with thinner channels. However, the median I_{ON}/I_{OFF} value was found to be very poor, namely, ~2, ~68 and ~3 for the $MoSe_2$ FETs with thicker channels for V, Nb and Ta dopants, respectively, whereas all the thinner channel FETs demonstrated $I_{ON}/I_{OFF} > 10^4$, irrespective of the dopant type. Similar results were obtained for doped WSe_2 FETs (Extended Data Fig. 3). Additionally, the schematic for thin- and thick-channel 2D FETs is included in Supplementary Fig. 2 for better understanding.

To comprehend the FET characteristics that vary with the thickness of the doped $MoSe_2$ layers, we conducted DFT-driven band structure calculations. These calculations reveal the precise position of the Fermi level (E_F) in the doped $MoSe_2$ samples. Supplementary Fig. 3a–d shows the atomic structures used for DFT simulation and Fig. 2a–d shows the calculated electronic band structure for pristine and V-, Nb- and Ta-doped 2H-phase $MoSe_2$ for single-layer (1L), double-layer (2L) and eight-layer (8L) configurations. Although 1L-$MoSe_2$ exhibits a direct (K–K) E_G of ~1.44 eV, 2L- and 8L-$MoSe_2$ display indirect (Γ–K) E_G of ~1.09 eV and ~0.91 eV, respectively, which are consistent with previously documented findings[24–27]. The intrinsic E_F, as expected, was located mid-gap, irrespective of the layer thickness in pristine $MoSe_2$. However, E_F was found to be shifted below the valence band maximum (E_V) near the K point of the Brillouin zone for 1L-$MoSe_2$, and at the Γ point for both 2L- and 8L-$MoSe_2$ for V-, Nb- and Ta-doped crystals. Although the exact location of E_F differed across the dopant types and layer numbers (Extended Data Fig. 4), the consistent observation of E_F being positioned below E_V confirmed the degenerate p-type doping of $MoSe_2$ for each of V, Nb and Ta dopants at ~3% atomic doping, which were used for the DFT calculations.

Figure 2e shows ($E_V - E_F$) for different layer thicknesses for each of the dopants. Clearly, the shift in E_F is more prominent in 8L- and 2L-$MoSe_2$ compared with 1L-$MoSe_2$ for all the dopant types. For

https://doi.org/10.1038/s41928-024-01265-2

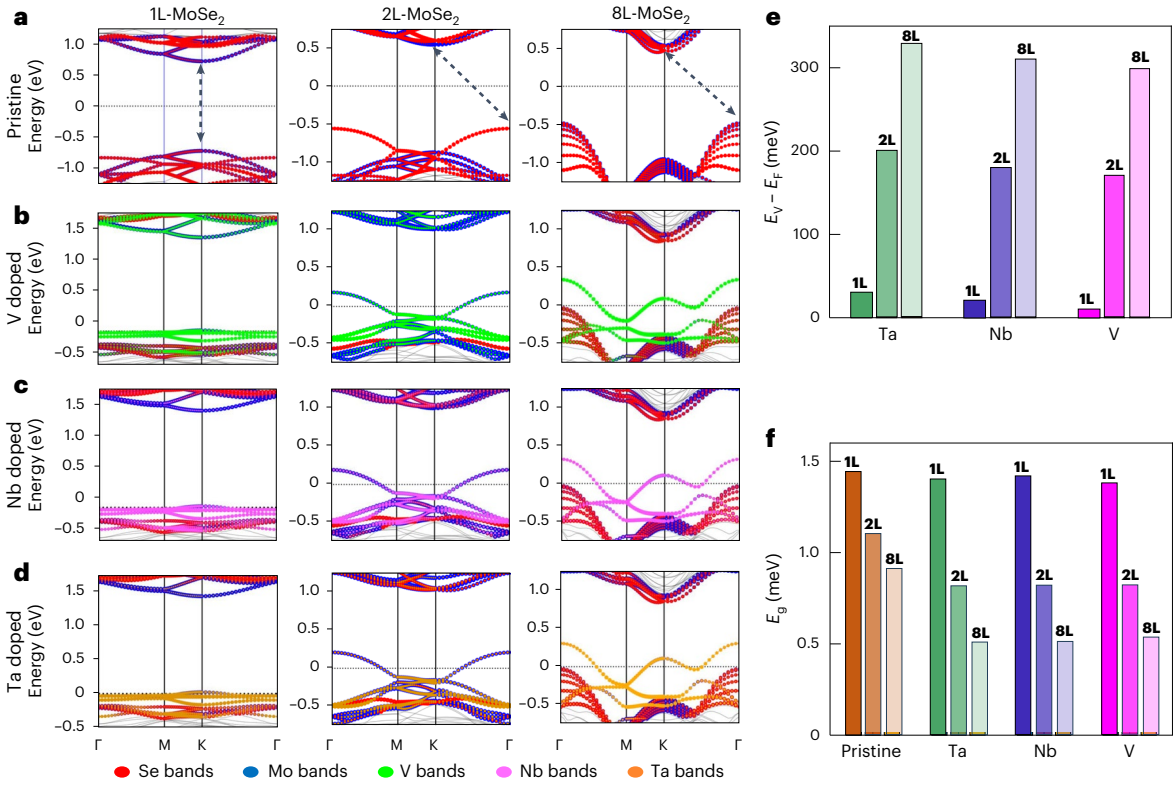

Fig. 2 | Electronic band structure of pristine and doped $MoSe_2$. a–d, Band structure of pristine (**a**) and V-doped (**b**), Nb-doped (**c**) and Ta-doped (**d**) 2H-phase $MoSe_2$ for 1L, 2L and 8L optimized structure. **e**, Bar plot showing the relative position of E_F with respect to E_V, that is, $E_V - E_F$ for 1L, 2L and 8L-$MoSe_2$ for each of the group VB dopants. **f**, Bar plot showing E_G for pristine as well as V-, Nb- and Ta-doped $MoSe_2$ for each thickness.

example, in the case of Nb doping, ($E_V - E_F$) is ~30 meV, ~200 meV and ~300 meV for 1L-, 2L- and 8L-$MoSe_2$, respectively. This can be explained from the shifts in the electronic band structure caused by the QCE in thinner layers[28]. In addition, although the pristine band structure of 1L-, 2L- and 8L-$MoSe_2$ remained largely intact after doping, a reduction in the magnitude of E_G is evident in doped $MoSe_2$ (Fig. 2f). For example, E_G values were found to be reduced from 0.9 eV to 0.53 eV and from 0.51 eV and 0.5 eV for V-, Nb- and Ta-doped 8L-$MoSe_2$. This effect stems from the disparity in atomic radii between the Mo atom and TM dopants, leading to lattice strain. The E_G narrowing is proportional to the amount of strain, which is directly connected to the atomic radii, with V having the smallest atomic radius and Ta having the largest. Similar trends were observed for 2L- and 1L-$MoSe_2$, too. However, as evident, the impact of strain-induced E_G narrowing is found to be minimal for 1L-$MoSe_2$. These observations also align with the results obtained from the analysis of the projected density of states (Supplementary Fig. 4). It is also worth mentioning that although the QCE impacts the positions of E_V and E_C, the energetic positions of the dopant states, which are localized in the material layers, are less affected by the QCE compared with the band edges. As a result, the energy gap between the dopant states and band edges increases as the layer thickness decreases, which, in turn, lowers the efficiency of dopant activation[20,21]. The DFT results, however, fail to account for the absence of degenerate doping in experimental devices featuring thin channels. This discrepancy arises due to the highly elevated (>10 times) doping concentration used in DFT simulations at 3% atomic doping, amounting to over ~30,000 ppm, which stands in contrast to the doping concentrations achieved in actual synthesized crystals. This deliberate adjustment was made to reduce the computational demands, given that the size of the unit cell used for DFT calculations becomes unmanageably large when the dopant concentration is too minimal. However, DFT calculations are able to confirm the experimental observation on layer-thickness-dependent doping efficacy in $MoSe_2$.

Extended Data Fig. 5a–d shows the field-effect mobility values (μ_{FE}) for holes extracted from the peak transconductance for V-, Nb- and Ta-doped $MoSe_2$ and WSe_2 FETs. We found that the thicker flakes have better μ_{FE} values in the range of 5–10 $cm^2 V^{-1} s^{-1}$ for both Nb- and Ta-doped $MoSe_2$ and WSe_2. In comparison, thinner flakes were found to possess $\mu_{FE} < 3$ $cm^2 V^{-1} s^{-1}$. This can be attributed to the higher R_C values associated with thinner flakes. We also found lower μ_{FE} values for V-doped samples irrespective of the flake thickness for both $MoSe_2$ and WSe_2. Since the μ_{FE} values are known to be prone to measurement artefacts[29], we also extracted the four-point probe (4PP) mobility for the bulk samples using Hall measurements. Extended Data Fig. 5e,f shows the μ_{4PP} values for V-, Nb- and Ta-doped $MoSe_2$ and WSe_2. Although the specific values vary, the μ_{FE} and μ_{4PP} measurements were observed to be in a comparable range.

Impact of degenerate doping on contact resistance

As mentioned earlier, degenerate doping has played a crucial role in optimizing the performance of Si FETs by reducing R_C, improving carrier injection efficiency and enhancing overall device characteristics. Supplementary Fig. 5a,b shows the SEM image and schematic of a representative transfer length method (TLM) structure used for extracting R_C from $MoSe_2$ FETs with Pd/Au contacts. Figure 3a shows the transfer characteristics of the best-performing V-, Nb- and Ta-doped thick $MoSe_2$ FETs taken at $V_{DS} = 1$ V, for $L_{CH} = 50$ nm, 100 nm, 200 nm and 500 nm. Note that Nb- and Ta-doped p-type $MoSe_2$ FETs can achieve I_{ON} as high as 1.8 mA μm^{-1} and 0.83 mA μm^{-1}, respectively, for $L_{CH} = 50$ nm, although weak electrostatic gate control leads to poor I_{ON}/I_{OFF}. Figure 3b shows the total resistance R_T (normalized by width) measured at $V_{BG} = -8$ V versus L_{CH} for these V-, Nb- and

https://doi.org/10.1038/s41928-024-01265-2

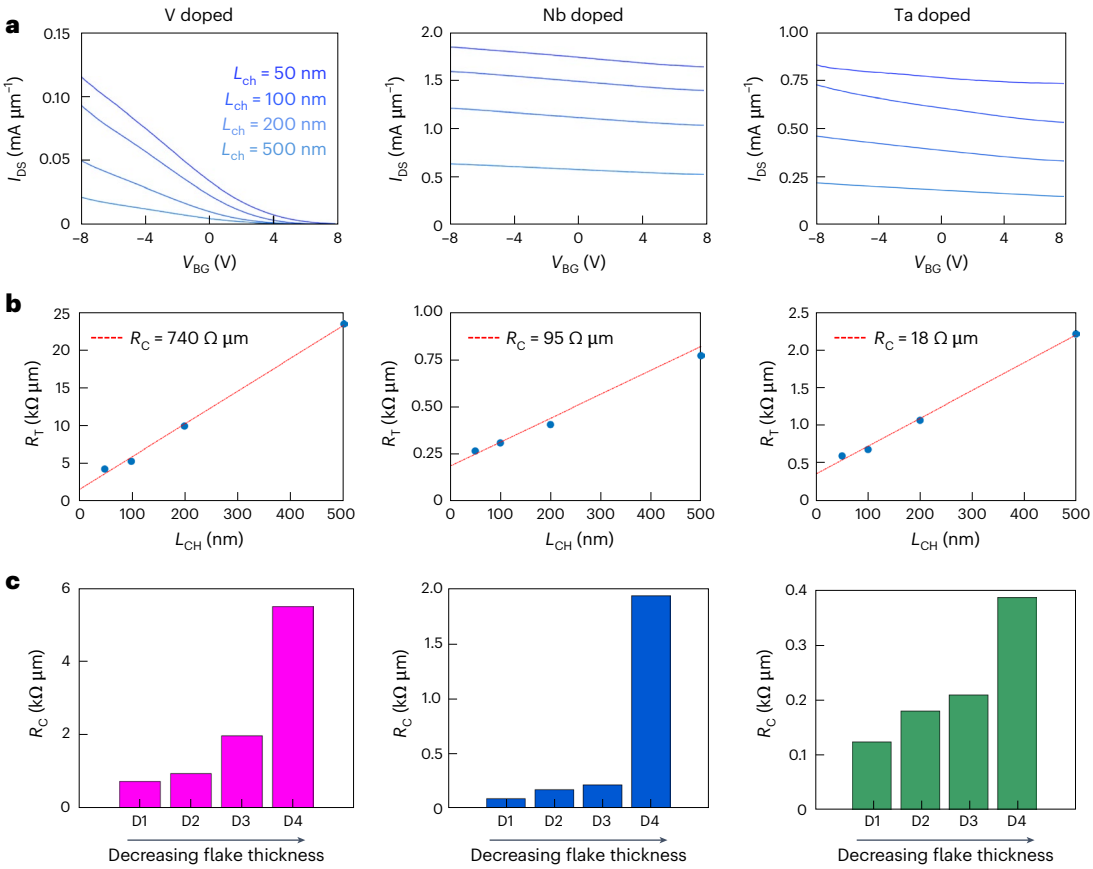

Fig. 3 | Impact of degenerate doping on contact resistance. a, Transfer characteristics of V-, Nb- and Ta-doped thick $MoSe_2$ flakes for different L_{CH} values. **b**, Corresponding TLM data, that is, R_T versus L_{CH} obtained at V_{BG} = −8 V along with the linear fits to extract the $2R_C$ values from the *y* intercepts. **c**, R_C values obtained from the TLM measurements for V-, Nb- and Ta-doped $MoSe_2$ flakes with different thicknesses. D1, >10 layers; D2, 8–10 layers; D3, 5–8 layers; D4, <5 layers.

Ta-doped thick $MoSe_2$ FETs, respectively. Next, equation (2) is used to extract R_C.

$$R_T = R_{CH} + 2R_C; R_{CH} = R_{SH}L_{CH} \quad (2)$$

As indicated in equation (2), R_{CH} decreases as L_{CH} is scaled. R_C, however, is independent of L_{CH} and can thus be extracted from the *y* intercept of the given R_T versus L_{CH} plots, although as $2R_C$. The slope of the linear-fit line represents the sheet resistance (R_{SH}). Figure 3c shows the bar plot for R_C extracted for V-, Nb- and Ta-doped $MoSe_2$ FETs with different flake thicknesses. It is important to recognize that for sufficiently thick flakes (>10 layers), the R_C values for V-, Nb- and Ta-doped $MoSe_2$ can be as low as ~740 Ω μm, 95 Ω μm and 125 Ω μm, respectively. Supplementary Fig. 6 displays I_{ON} as a function of L_{CH} for a supply voltage of V_{DD} = 1 V following equation (2) for these lowest R_C values obtained experimentally. Note that even with an R_{SH} value as high as 10 kΩ μm, achieving an I_{ON} > 1 mA μm^{-1} is feasible for Nb- and Ta-doped $MoSe_2$ FETs when the channel length is reduced to L_{CH} < 15 nm. These findings highlight the importance of degenerate doping in lowering R_C to meet the International Roadmap for Devices and Systems requirements for high-performance FETs in advanced technology nodes.

A 2D FET design with variable channel thickness

We provide a design aimed at optimizing the performance of p-type 2D FETs by carefully manipulating three key parameters: low R_C, high I_{ON} and precise gate control to achieve high I_{ON}/I_{OFF}. This approach involves tailoring the thickness of the 2D channel material to achieve the desired outcomes. Drawing from our experimental findings, where low R_C was observed in thicker, multilayered Nb-doped $MoSe_2$ and enhanced gate control was achieved in its monolayer form, we propose a transistor architecture that combines these advantages. As shown in Fig. 4a, our proposed design involves maintaining a thicker multilayer structure (~4–6 layers) beneath the source and drain contacts, ensuring the central channel region between the contacts remains thin (~1–3 layers) to preserve effective gate control. To achieve controlled thinning of substitutionally doped multilayered 2D materials, we use a self-limiting etching technique. Specifically, we utilize mild radio-frequency-plasma-based oxidation of the top layer, resulting in the formation of a passivating and sub-stoichiometric MoO_3 layer that can be selectively dissolved in deionized water. This technique allows for a layer-by-layer removal of the 2D channel region between the contacts, leaving the material beneath the contacts untouched. Extended Data Fig. 6a shows the optical images confirming the layer-by-layer thinning of Nb-doped multilayer $MoSe_2$ flakes. Additionally, Extended Data Fig. 6b presents the atomic force microscopy (AFM) images alongside their respective height profiles for another multilayer Nb-doped $MoSe_2$ flake subjected to five rounds of the plasma thinning process. Evidently, there is a reduction in layer thickness of approximately 0.8 nm after each etching cycle, which substantiates the occurrence of layer-by-layer etching.

A visual representation of the final prototype 2D FET device is presented in Fig. 4b using the cross-sectional scanning transmission electron microscopy (STEM) image in the high-angle annular dark-field mode and the accompanying EDS elemental mapping. The channel remains thick (~six monolayers) beneath the source and drain contacts and thin (three monolayers) between the contacts. Note that we carried out three successive rounds of oxygen plasma treatment, followed by immersion in water. Supplementary Fig. 7 shows the high-angle annular

https://doi.org/10.1038/s41928-024-01265-2

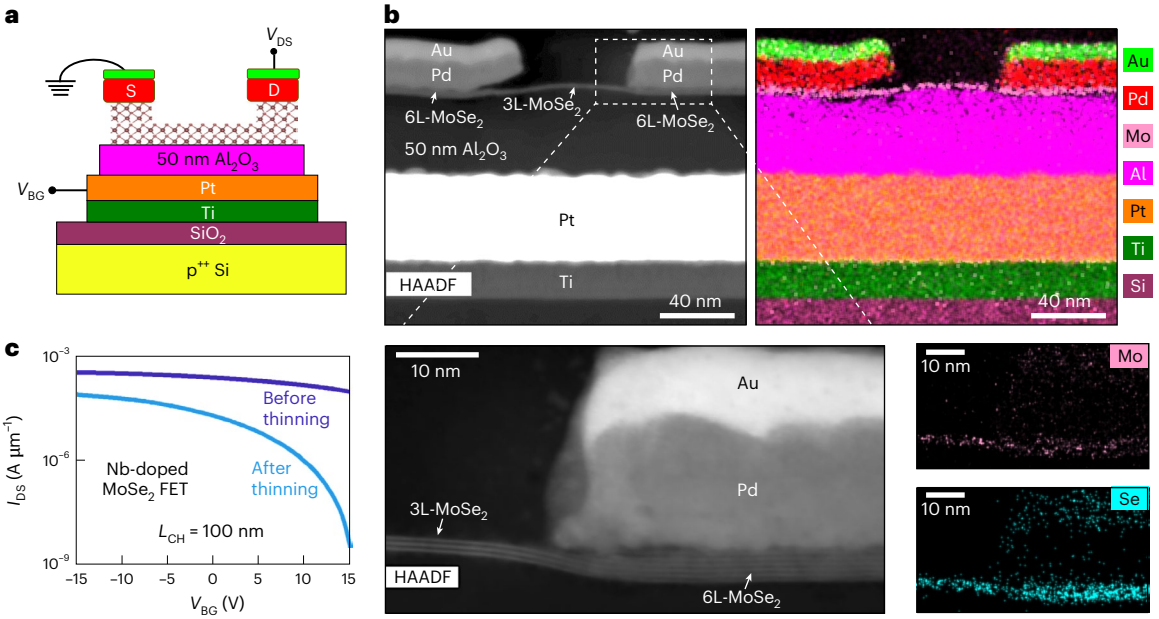

Fig. 4 | A 2D FET design with variable channel thickness. a, Schematic of our proposed 2D FET architecture involving a thicker multilayer (~4–6 monolayers) channel beneath the source and drain contacts, and a thinner channel (~1–3 monolayers) region between the contacts. The thicker channel enables degenerate p-type doping and therefore reduced R_C and enhanced I_{ON}, whereas the thin channel ensures precise electrostatic gate control, resulting in high I_{ON}/I_{OFF}. **b**, Cross-sectional high-angle annular dark-field (HAADF) STEM image and the accompanying EDS elemental mappings of the fabricated prototype 2D FET device. The channel maintains a thickness of approximately six monolayers beneath the source and drain contacts, and is thinner (three monolayers) between these contacts. Three consecutive cycles of oxygen plasma treatment, followed by immersion in water, were carried out to thin the central channel region layer by layer. **c**, Transfer characteristics of the Nb-doped $MoSe_2$ FET before and after plasma treatment for L_{CH} = 100 nm. The ON-state performance is largely retained, with high I_{ON} of 85 μA μm^{-1} at V_{DS} = 1 V, whereas the I_{ON}/I_{OFF} is substantially enhanced from ~3×10^4 to ~4×10^4.

dark-field STEM image of the entire TLM structure with thick channels underneath the contacts and thinned-down channels between the contacts. The resulting transfer characteristics of the Nb-doped $MoSe_2$ FET before and after plasma treatment are shown in Fig. 4c for L_{CH} = 100 nm. Clearly, the ON-state performance is largely retained, whereas the I_{ON}/I_{OFF} value is enhanced from 3×10^4 to around 4×10^4. Extended Data Fig. 7a–c shows the transfer characteristics of the Nb-doped $MoSe_2$ FET for different L_{CH} values and the extracted R_C values before and after the plasma treatment. Clearly, R_C, which is a major hurdle in achieving efficient p-type FET performance, remains consistently low even after the controlled layer-by-layer thinning. The R_C value was found to be around 2 kΩ μm, resulting in I_{ON} of 85 μA μm^{-1} for a device with L_{CH} = 100 nm at V_{DS} = 1 V and for a carrier concentration of $n_S \approx 2 \times 10^{13}$ cm^{-2}. Similar results were also obtained for Ta-doped $MoSe_2$ FETs (Supplementary Fig. 8). Here the ON-state performance is largely retained, whereas the I_{ON}/I_{OFF} value is substantially enhanced from ~15 to ~10^4 after thinning the channel regions between the contacts. The R_C value for post-processed Ta-doped $MoSe_2$ FETs was found to be around 5 kΩ μm, resulting in high I_{ON} of ~100 μA μm^{-1} for a device with L_{CH} = 100 nm at V_{DS} = 1 V. The increases in R_C after the channel-etching process can be explained using a simple resistor network model (Extended Data Fig. 8).

High-performance dual-gated p-type 2D FET

To further improve the performance of our proposed p-type 2D FET, we have scaled the channel length down to L_{CH} = 50 nm and improved the electrostatic control of the channel by introducing a dual-gated device geometry. Figure 5a–d shows the schematic, cross-sectional high-resolution transmission electron microscopy (TEM) image of a representative dual-gated Nb-doped $MoSe_2$ FET with a thicker channel underneath the source/drain contacts and thinner channel between the contacts with accompanying EDS elemental mapping. We used 20-nm- and 25-nm-thick ALD-grown Al_2O_3 as the top- and bottom-gate dielectrics, respectively. We used Pt/Ti and Ni/Au as the bottom- and top-gate electrode, and Pd/Au as the source/drain metal contacts. Using metals with high work functions for the source, drain and gate electrodes provides the optimal opportunity to realize high-performance p-type 2D FETs.

Figure 5e shows a series of transfer characteristics of a representative dual-gated FET, with the structure shown in Fig. 5a, where V_{BG} is swept from −8 V to 8 V and the top-gate voltage (V_{TG}) is stepped from −10 V to 10 V. Note that the highest I_{ON} value is achieved when both the bottom- and top-gate voltages are negative, allowing maximum charge accumulation in the channel. Similarly, the highest I_{ON}/I_{OFF} is obtained when both the bottom- and top-gate voltages are positive, allowing maximum charge depletion in the channel. In other words, when both gates work in conjunction, it is possible to achieve better electrostatic control of the channel compared with a single gate. Figure 5f shows the transfer characteristics of the same devices when the top and bottom gates are shorted, and the voltage applied to the dual gate (V_{DG}) is swept from −10 V to 10 V. The dual-gated Nb-doped $MoSe_2$ FETs with a thin channel between the contacts and thicker channel underneath the contacts are able to demonstrate I_{ON} = 212 μA μm^{-1} and simultaneously display $I_{ON}/I_{OFF} = 10^4$. Figure 5g,h shows the bar plots for I_{ON} and I_{ON}/I_{OFF} for several p-type 2D dual-gated FETs. The median I_{ON} and I_{ON}/I_{OFF} values are 160 μA μm^{-1} and 4.4×10^3, respectively.

We also wish to highlight the value of successfully implementing a dual-gated 2D FET in the 2D device community. First, the challenge of depositing high-quality ALD films on 2D materials is substantial, primarily due to the inert nature of their basal planes. Second, although there have been some reports on successful top-gate device fabrication, there is often a disparity in the electrostatic strength between the top and bottom gates. This discrepancy is usually attributed to thicker and low-κ back-gate dielectric, which leads to a higher effective oxide thickness, compared with the thinner and high-κ top-gate dielectric that offers a lower effective oxide thickness. Such differences hinder effective dual-gate operation, as applying the same voltage to both

https://doi.org/10.1038/s41928-024-01265-2

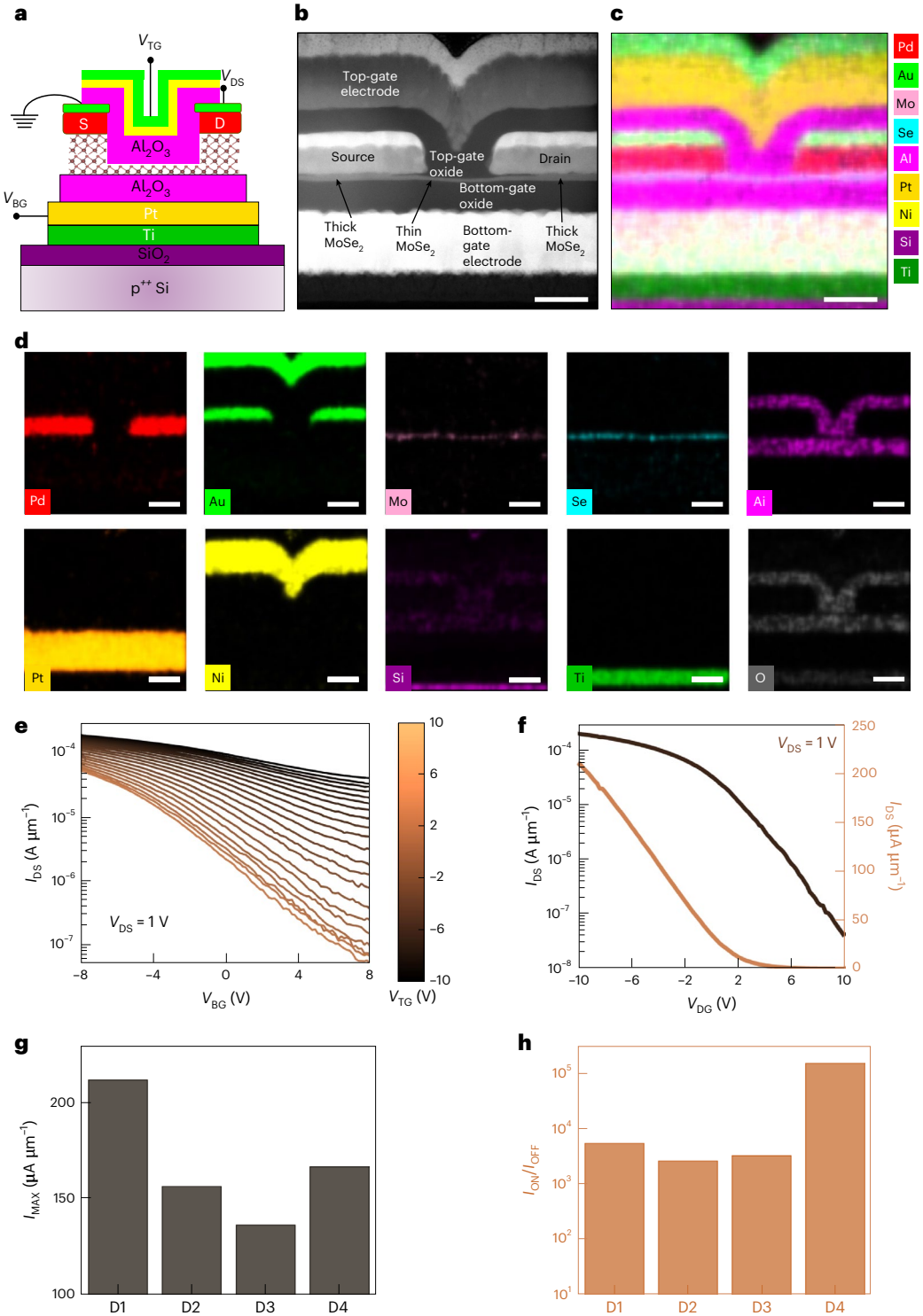

Fig. 5 | High-performance p-type dual-gated 2D FET. a–**c**, Schematic (**a**), cross-sectional high-resolution STEM image (**b**) and EDS elemental mapping (**c**) of a representative dual-gated Nb-doped $MoSe_2$ FET with a thicker channel underneath the source/drain contacts and a thinner channel between the contacts. **d**, Mass percent elemental mapping for each element in the dual-gated FET structure. **e**, Transfer characteristics of a representative FET with the structure presented in **a**, where V_{BG} is swept from −8 V to 8 V and V_{TG} is stepped from −10 V to 10 V. The drain bias was 1 V. **f**, Transfer characteristics of the same devices in both linear and logarithmic scales when the top and bottom gates are shorted and V_{DG} is swept from −10 V to 10 V with an applied drain bias of 1 V. **g**, Bar plot illustrating the maximum ON current (I_{ON}) for four devices, with the highest I_{ON} value reaching 212 μA μm^{-1} and median I_{ON} value of 160 μA μm^{-1}. **h**, Corresponding I_{ON}/I_{OFF} ratio for each device, with the highest I_{ON}/I_{OFF} value reaching 10^5 and median I_{ON}/I_{OFF} value of 3.3×10^4. All scale bars are 40 nm.

gates is not feasible. This Article demonstrates that a comparable electrostatic strength between the top and bottom gates can be achieved in dual-gated 2D FET. This method allows for improved control, leading to the development of p-type 2D FETs that outperform previously reported ones[30]. However, there remains room for improving the median I_{ON} and I_{ON}/I_{OFF} values reported in this work. The key to improve the p-type FET performance still lies in improving the gate stack interface resulting in a near-ideal subthreshold swing as well as a low threshold voltage.

https://doi.org/10.1038/s41928-024-01265-2

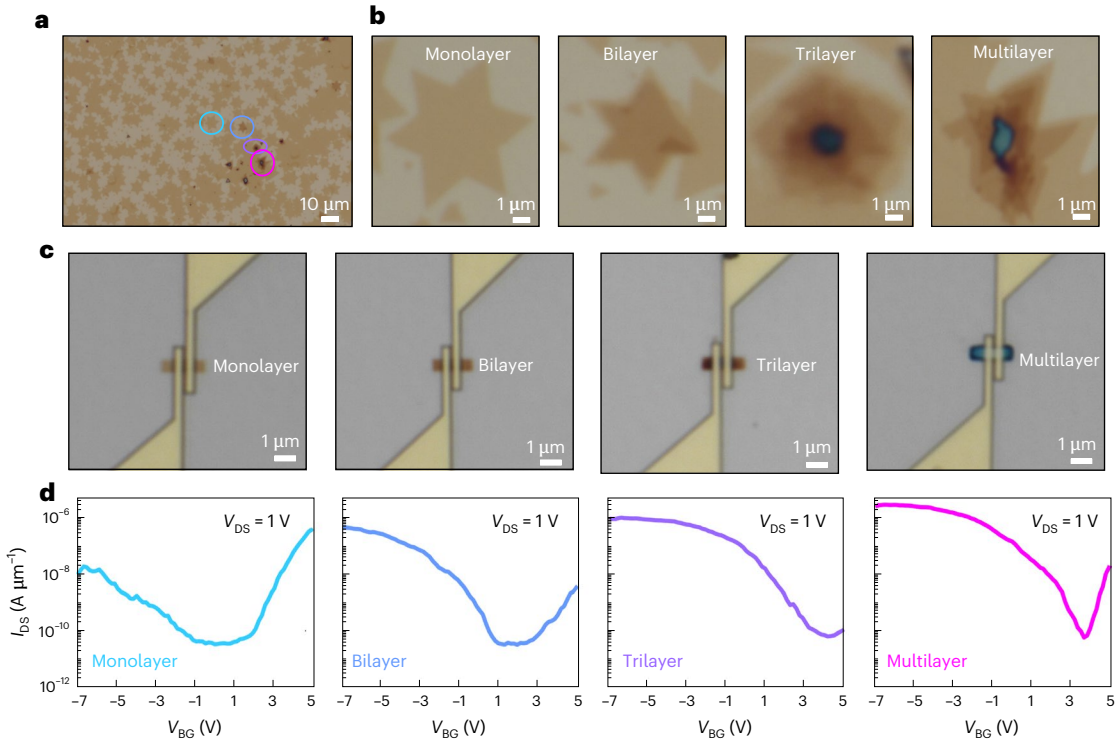

Fig. 6 | Electrical characterization of Nb-doped CVD-grown large-area $MoSe_2$ FETs. a, ×20 optical image of a Nb-doped large-area $MoSe_2$ film grown using CVD. The film predominantly consists of monolayers with some bi-, tri- and multilayer regions. **b**, The ×100 optical image of each of the mono-, bi-, tri- and multilayer regions is shown. **c**,**d**, Optical image (**c**) and transfer characteristics (**d**) of FETs fabricated with mono-, bi-, tri- and multilayer Nb-doped $MoSe_2$ as the channel. The devices have an L_{CH} = 200 nm and W_{CH} = 1 μm at V_{DS} = 1 V. Although monolayer $MoSe_2$ FETs showed stronger n-type transport compared with p-type transport, with increasing thickness of the film, the FETs exhibited a distinct p-type behaviour. This can be attributed to the presence of larger concentrations of Nb atoms in the multilayered films.

Supplementary Fig. 9a,b shows the output characteristics of a high-performance Nb-doped $MoSe_2$ FET measured at T = 25 K and 300 K, respectively. The output characteristics exhibit more Schottky-type behaviour at 25 K and become linear at 300 K. We extracted the SB heights for hole injection ($\phi_{SB\text{-}P}$) in pristine and V-, Nb- and Ta-doped $MoSe_2$ and WSe_2 for Pd contacts (Extended Data Fig. 9a,b). The $\phi_{SB\text{-}P}$ values were found to be ~500 meV for $MoSe_2$ and ~800 meV for WSe_2 with Pd contacts, regardless of the dopant type. This is expected since doping does not typically change the SB height at metal–semiconductor contacts, which is primarily determined by the work function of the contact metal and the electron affinity or bandgap of the semiconductor. However, doping does impact the SB width ($\lambda_{SB\text{-}P}$) at the metal–2D contact interface, with heavier doping resulting in a narrower barrier, as illustrated using energy band diagrams (Extended Data Fig. 9c,d). Additionally, Extended Data Fig. 9e presents the output characteristics at small drain biases, ranging from −100 mV to 100 mV, across different temperatures ranging from 75 K to 300 K. A noticeable increase in linearity with temperature is observed, which can be attributed to the temperature-assisted tunnelling process at the metal–2D contact interfaces with large SB heights. At higher temperatures, Fermi-level broadening allows more carriers to tunnel through the thinner part of the SB, increasing the tunnelling current and giving the output characteristics a more linear appearance. This observation challenges a common misconception in the field that linear output characteristics results from ohmic contacts. Even at low temperatures, the output characteristics can appear linear for an SB contact if sufficient tunnelling is enabled—a result of $\lambda_{SB\text{-}P}$ reduction through degenerate doping.

Towards large-area doped p-type 2D FETs

Although our study on exfoliated flakes can guide the materials science field towards focusing on key areas relevant to device research, we recognize the scalability limitations of the CVT method. Therefore, we have made some preliminary efforts on growing Nb-doped $MoSe_2$ using the chemical vapour deposition (CVD) technique, as evident from the optical image shown in Fig. 6a. It should be noted that although the film is predominantly monolayer, there are also regions with bilayer, trilayer and multilayer structures (Fig. 6b). The growth details are provided in the Methods. Supplementary Fig. 10 shows the Raman and photoluminescence (PL) spectra obtained from the mono-, bi-, tri- and multilayer regions of the Nb-doped $MoSe_2$ film, indicating the high quality of CVD-grown $MoSe_2$ films. Next, we transferred these films onto a global back-gate substrate with a 25-nm-thick layer of ALD-grown Al_2O_3 and constructed FETs with L_{CH} of 200 nm and width of 1 μm (Fig. 6c). Although degenerate doping was not observed in films of any channel thickness, a distinct pattern emerges in the transfer characteristics with an increase in channel thickness (Fig. 6d). The monolayers exhibit stronger n-type than p-type conduction, but as we move to bilayer, trilayer and multilayer structures, the p-type conduction intensifies, with multilayers displaying the highest I_{ON} value at 5 μA μm^{-1}. We believe that the concentrations of Nb dopant in these films were not high enough to cause degenerate doping. Nonetheless, the findings from CVD-grown large-area films align with our findings on exfoliated flakes and DFT calculations. Both studies suggest the diminishing effectiveness of dopants as the layer thickness decreases. In other words, for achieving degenerately doped contact regions, the growth of multilayer films is important. In our future work, we will aim to optimize the CVD growth of multilayer and doped $MoSe_2$ films.

Benchmarking

A benchmarking table showing the advances demonstrated in this work over previous attempts at achieving high-performance p-type 2D FETs is provided in Extended Data Table 1. Noteworthy among

these findings is the work[31] in which surface charge transfer doping technique based on an ultrathin MoO_3 layer synthesized through flame-based methods serving as a hole-doping layer for WSe_2 FETs. An I_{ON} value of 100 μA μm^{-1} was achieved owing to a relatively low R_C value of 0.8 kΩ μm. However, the degenerate p-type doping greatly reduced the ON/OFF current ratio (~10). In comparison, our results on Ta-doped $MoSe_2$ FETs have achieved a high I_{ON} value of 527 μA μm^{-1} owing to an R_C value of only 0.4 kΩ μm with a similar I_{ON}/I_{OFF} current ratio of ~15. In a more recent work[32], NO_x treatment was used to dope the complete channel region of a monolayer WSe_2 FET, achieving a remarkable I_{ON} value of 300 μA μm^{-1}, a high ON/OFF current ratio of 2×10^6 and a low R_C value of 0.95 kΩ μm. Although this method holds significance, its applicability is limited to WSe_2, and its feasibility for other 2D materials remains to be tested. Another work[30] reported CVD-grown monolayer WSe_2 with Sb/Pt contact and combined it with oxide-based encapsulation/doping technology to reach $I_{ON} \approx 150$ μA μm^{-1} and an R_C value of 0.75 kΩ μm. Without the encapsulation layer, the I_{ON} value decreased to around 25 μA μm^{-1}. In comparison, our work achieved $I_{ON} \approx 212$ μA μm^{-1}, without the use of an encapsulation layer. This distinction is important because the presence of encapsulation layers can hinder the fabrication of top gates, which is ultimately needed for circuit design. Besides the surface charge transfer doping approaches, the successful demonstrations of substitutional p-type doping in 2D TMDs have been achieved using TMs like Nb, Ta, V and others[33–39]. However, none of these studies were able to achieve an I_{ON} value as high as that reported for our Nb-doped dual-gated $MoSe_2$ FETs, featuring thin channels between the contacts and thicker channels underneath the contacts.

Conclusions

We have examined the effect of different thicknesses of pristine and doped $MoSe_2$ and WSe_2 crystals on 2D FETs. Pristine flakes exhibited n-type transport, whereas thick doped flakes (>6 layers) exhibited degenerate p-type doping with enhanced I_{ON} (as high as 1.8 mA μm^{-1}) and reduced R_C (as low as 95 Ω μm), but poor I_{ON}/I_{OFF} (<20). In contrast, thinner flakes (1–3 layers) exhibited high I_{ON}/I_{OFF} (>10^5) but low I_{ON} due to high R_C. We, thus, created p-type Nb-doped $MoSe_2$ FETs with combined high I_{ON}, low R_C and large I_{ON}/I_{OFF} (85 μA μm^{-1}, 2 kΩ μm and 10^4, respectively) by designing devices in which the semiconductor is around 1–3 layers in the channels and >6 layers under the contact region. Furthermore, we combined this strategy with channel-length scaling and dual-gated architecture to achieve an I_{ON} value as high as 212 μA μm^{-1}. We also demonstrated layer-thickness-dependent doping efficacy in large-area Nb-doped $MoSe_2$ grown via CVD. Our approach could be extended to various 2D materials, accommodating n- and p-type doping, as well as large-scale synthesis. The work also highlights the importance of considering doped multilayer materials in the development of 2D FET technology, as well as the typical focus on monolayer approaches.

Methods

DFT calculations

To model the investigation of substitutional doping by group VB elements in the 2H phase of $MoSe_2$, all the DFT computations were executed using the Kohn–Sham Hamiltonian. The utilized exchange–correlation functionals were outlined under the generalized gradient approximation, following the Perdew–Burke–Ernzerhof description[40], which we implemented in the Virtual Nanolab QuantumATK (2022.12-SP1)[41]. To optimize the lattice structure, we used an energy cut-off of 125 hartree, alongside a k-grid sampling of $5 \times 5 \times 1$. This approach considers electrons residing in Mo ($5s^1 4d^5$), selenium (Se) ($4s^2 4p^4$), Nb ($4d^5 5s^1$), V ($3d^3 4s^2$) and Ta ($5d^3 6s^2$) orbitals as the valence electrons. To simulate doping by group VB elements in $MoSe_2$, we constructed ($5 \times 5 \times 1$), ($4 \times 4 \times 2$) and ($2 \times 2 \times 8$) hexagonal supercells for 1L-, 2L- and 8L-$MoSe_2$, respectively. In these structures, we selectively replaced one Mo atom with a group VB atom, resulting in the creation of $Mo_{24}(D)Se_{50}$, $Mo_{31}(D)Se_{64}$ and $Mo_{31}(D)Se_{64}$ arrangements, where D signifies the dopant atom. This group VB atom substitution corresponds to a doping percentage of 4.12% in 1L-$MoSe_2$ and 3.12% in both 2L- and 8L-$MoSe_2$. Furthermore, the influence of van der Waals forces in 2L- and 8L-$MoSe_2$ was considered by including Grimme's DFT-D2 dispersion-correction method. Structures were optimized to minimize the total energy until atom forces were below 0.01 eV Å^{-1}, with a tolerance limit of 10^{-5} using a limited-memory Broyden–Fletcher–Goldfarb–Shannon method. High-symmetry k points (Γ–M–K–Γ) were used for the band structure calculation. Here our objective is to find appropriate group VB element dopants capable of creating p-type doping in $MoSe_2$ for FET applications. The effect of spin–orbit coupling was not considered in the band structure calculation. It is noted that spin polarization is necessary to understand the magnetic properties of TM-doped $MoSe_2$.

2D material growth by CVT

Crystals of $MoSe_2$, WSe_2 and doped counterparts were prepared by the CVT method in a quartz glass ampoule using $SeCl_4$ as a transport agent. For the synthesis, 3 at.% of dopant ($W(Mo)_{0.97}DOP_{0.03}Se_{2.02}$) (DOP denotes the different dopants used) was used and excess of Se to reduce the vacancy density in the growth crystals. For the undoped crystal, growth was done using the $W(Mo)Se_{2.02}$ composition. The mixture of elements (W, +99.999%, −100 mesh; Mo, +99.999%, −100 mesh; Se, +99.9999%, 2–4 mm granules; Ta, +99.9%, −100 mesh; Nb, +99.9%; V, +99.9%, −100 mesh) corresponding to 50 g were placed in an ampoule (50 mm × 250 mm) together with 0.5 g $SeCl_4$ (99.9%) inside a glovebox and melt sealed under a high vacuum (diffusion oil pumping with LN_2 trap; <1×10^{-3} Pa) using an oxygen–hydrogen welding torch. The ampoule was placed in a muffle furnace and heated at 500 °C for 25 h, at 600 °C for 50 h and at 800 °C for 50 h. The heating and cooling rates were 1 °C min^{-1} and between each temperature step, the reaction mixture was homogenized by shaking for 5 min. The formed polycrystalline diselenide was placed in a two-zone horizontal crystal growth furnace for CVT crystal growth. First, the growth zone was heated at 1,000 °C and the source zone was kept at 700 °C. After 50 h, the thermal gradient was reversed, and the source zone was kept at 1,000 °C as the temperature of the growth zone was reduced from 950 °C to 900 °C over a period of 10 days. Finally, the growth zone was heated to 500 °C for 2 h to remove the transport medium and excess Se from the growth crystals. Over a 10-day period, over 40 g crystals were obtained. The ampoules were opened in an argon-filled glovebox and the crystals were stored under an inert atmosphere.

2D material growth by CVD

A Nb-doped $MoSe_2$ film was synthesized using liquid-phase precursor-assisted CVD[42,43]. The film was grown in a two-zone furnace on Si/SiO_2 substrates with a 300 nm oxide layer. Metal precursors consisted of a combination of a Mo-based solution and Nb-based solution. The Mo-based solution consists of 1:4 volume ratio of ammonium molybdate tetrahydrate ($(NH_4)_2MoO_4 \cdot 4H_2O$) and sodium cholate hydrate ($C_{24}H_{39}NaO_5 \cdot xH_2O$) in deionized water. The Nb-doping solution is a mixture of ammonium niobate oxalate hydrate ($C_4H_4NNbO_9 \cdot xH_2O$) and deionized water. After spin coating the metal precursor onto a Si/SiO_2 substrate, it was placed in a quartz tube at the centre of the furnace. Simultaneously, 300 mg of Se powder was introduced in an Al_2O_3 boat at a second heating zone in the upstream region. The growth reaction occurred with the substrate temperature maintained at 800–825 °C for a 15 min period, whereas the Se heating zone was maintained at 375 °C. Here 100 s.c.c.m. Ar gas was used for ramping up the furnace and 200 s.c.c.m. Ar/H_2 (9:1) was used as the carrier gas during the growth period. After synthesis, the furnace naturally cooled down. The presence of $MoSe_2$ was confirmed with Raman and PL spectroscopy using a 532 nm laser in a Horiba LabRAM device.

Raman and PL spectroscopy measurements

Raman and PL spectroscopy measurements of the as-grown Nb-doped $MoSe_2$ film were performed on a Horiba LabRAM HR Evolution confocal Raman microscope with a 532 nm laser. The objective magnification was ×100 with a numerical aperture of 0.9, and the grating had a spacing of 1,800 gr mm^{-1} for Raman measurements and 300 gr mm^{-1} for PL measurements.

Hall bar measurements

Hall bar measurements were performed at room temperature using a DX-100 Hall effect system on bulk samples by making 4PP contacts with Cr/Au (van der Pauw geometry), as the magnetic field was swept from ±500 mT.

ICP-AES measurements

Bulk as-grown 2D material crystals were digested in acid. The acid solution was consequently nebulized into a fine aerosol, which was then introduced into a high-energy plasma (temperature between 7,000 K and 10,000 K). The plasma excites the atoms and ions to higher-energy levels. As they drop back down to their normal levels, they emit energy at wavelengths that are specific to the particular element. The wavelengths of emitted energy are separated in an optical chamber. By monitoring what wavelengths are emitted, we can determine how much of each element is present (quantitative determination).

EDS measurements

EDS analysis was carried out on micrometre-sized bulk flakes of crystals using an ESEM Q250 SEM instrument. An accelerating voltage of 30 kV with a tungsten source was used to detect the concentration of dopants in the crystals.

2D film transfer to target substrates

To fabricate the FETs, 2D TMD flakes were exfoliated on a 30 nm Au-coated silicon wafer. The flakes were then transferred from the Au substrate to the global back-gated Al_2O_3/Pt/Ti/p^{++}-Si substrate using a polymethyl methacrylate (PMMA)-assisted wet transfer process. First, the exfoliated TMD flakes on the Au substrate were spin coated with PMMA and baked at 150 °C for 2 min to ensure good PMMA/2D film adhesion. The corners of the spin-coated film were scratched using a razor blade and immersed inside a 1 M NaOH solution kept at 90 °C. Capillary action caused NaOH to be preferentially drawn into the substrate–film interface due to the hydrophilic nature of Au and the hydrophobic nature of the 2D film and PMMA, separating the PMMA/2D film from the Au substrate. The separated film was then fished from the NaOH solution using a clean glass slide and rinsed in three separate water baths for 15 min each before finally being transferred onto the target substrate. Subsequently, the substrate was baked at 50 °C and 70 °C for 10 min each to remove moisture and promote film adhesion, thereby ensuring a pristine interface, before the PMMA was removed using acetone immersion overnight and the film was cleaned with isopropyl alcohol.

2D FET fabrication

2D FETs were fabricated using ZEP520A 1:1 as the e-beam resist. The sample is initially dipped in SURPASS-4K for 60 s, rinsed in deionized water and then baked at 100 °C for 1 min. This is done to improve the adhesion of the resist to the substrate that contains exposed metal alignment markers. ZEP520A 1:1 was spun at 5,000 r.p.m. for 45 s and baked at 180 °C for 3 min (ref. 44). E-beam lithography is carried out at a beam energy of 100 keV and is developed in *n*-amyl acetate chilled at −10 °C for 3 min and isopropyl alcohol at room temperature for 60 s. Post-developing, 15 nm of Pd is evaporated using e-beam evaporation, which now serves as contacts to the 2D FETs.

Oxygen-plasma-based layer-thinning treatment

The substrate containing the flakes were exposed to radio-frequency-generated oxygen plasma in a TePla M4L dry etch system. Oxygen flow was set at 150 s.c.c.m. and helium at 50 s.c.c.m., which acts as the carrier gas for oxygen in the process. The chamber pressure was maintained at 550 mtorr and the sample was exposed to plasma at a radio-frequency power of 50 W for 15 s. Then, the sample was subsequently dipped in deionized water in a beaker for 2 min before drying with nitrogen.

Top-gated fabrication for 2D FETs

A 2-nm-thick layer of aluminium was deposited on the 2D FET by e-beam evaporation, which serves as the seed layer for ALD of the top-gate dielectric. Subsequently, a 20-nm-thick Al_2O_3 layer was grown with the seed layer by ALD. Next, the substrate was lithographically patterned using e-beam followed by the deposition of the top-gate electrode consisting of 20 nm Ni and 10 nm Au by e-beam evaporation. Finally, the regions above the source and drain contacts were lithographically patterned and exposed to reactive ion etching with BCl_3 to access the source–drain contact pads.

SEM measurements

SEM images of the 2D FETs were obtained using a ZEISS Gemini 500 field-emission SEM instrument with an accelerating voltage of 5 kV.

TEM sample preparation

Two thin TEM samples as shown in Figs. 4 and 5 were prepared using the Thermo Fisher Scientific Helios and Scios 2 DualBeam focused-ion-beam SEM device. These samples were first coated individually with a 0.5-µm-thick carbon layer using a 1.6 nA e-beam to protect the surface $MoSe_2$ layer from Ga-ion-beam damage. Subsequently, another carbon layer, approximately 4 µm thick, was deposited on top of each electron beam carbon layer using a 0.12 nA Ga ion beam. This layer served to protect the sample surface during ion-beam milling and sample thinning. Following this, a 2-µm-thick lamella of each sample cross-section around the electrode region was lifted out and in situ transferred to a copper half-grid. Each lamella was then thinned using a Ga ion beam at five decreasing voltage levels: 30 kV, 16 kV, 8 kV, 5 kV and 2 kV. As the lamellas became progressively thinner, the ion-beam voltage was gradually reduced to minimize damage.

STEM characterization of the cross-section

STEM and EDS characterizations were conducted on an aberration-corrected Thermo Fisher Scientific Titan3 FEI Titan3 G2 60-300 S/TEM instrument operating at an accelerating voltage of 300 kV, with spot size of 6, C2 aperture of 70 µm and convergent angle of 25.2 mrad. The EDS elemental maps were acquired using the SuperX EDS system (Bruker) under STEM mode. The double electrode STEM image and the corresponding EDS intensity plot (top panel of Fig. 4b) were taken under a beam current of 0.6 nA. Meanwhile, the enlarged single electrode STEM image and its associated EDS image in the bottom pannel of Fig. 4b and Fig. 5b–d, utilized a beam current of 0.07 nA to minimize sample damage while ensuring sufficient X-ray counts for analysis. The EDS images in Fig. 4b and Fig. 5c are intensity plots, whereas the individual elemental maps in Fig. 5d were mass percent plots quantified using Esprit software. This quantification involved 1/4 Q-Map preprocessing, the series fit method for deconvolution, the peak-to-background Cliff–Lorimer method for mass percent quantification and 4-pixel averaging for post-filtering, to enhance the accuracy and clarity of the elemental distributions. All elemental maps in Fig. 5d are adjusted with +40% brightness and +20% contrast in Microsoft PowerPoint software for better visualization.

AFM measurements

AFM was utilized to investigate the thickness profile of the exfoliated multilayer flakes before and after plasma treatments. RTESPA-150 probe tips were used with a Bruker Dimension Icon AFM device. All the images were collected in the peak-force tapping mode with a peak force of 12 nN and a scan rate of 0.5 Hz. Images were processed and exported using Gwyddion.

Electrical characterization

Electrical characterization of the fabricated devices was performed using a Lake Shore CRX-VF probe station in atmospheric conditions with a Keysight B1500A parameter analyser. Statistical measurements were performed using a semi-automated FormFactor 12000 probe station in atmospheric conditions with the Keysight B1500A parameter analyser.

Data availability

The data that support the findings of this study are available from the corresponding authors upon reasonable request.

Code availability

The codes used for plotting the data are available from the corresponding authors upon reasonable request.

References

1. Manzeli, S., Ovchinnikov, D., Pasquier, D., Yazyev, O. V. & Kis, A. 2D transition metal dichalcogenides. *Nat. Rev. Mater.* **2**, 17033 (2017).
2. Bhimanapati, G. R. et al. Recent advances in two-dimensional materials beyond graphene. *ACS Nano* **9**, 11509–11539 (2015).
3. Choi, W. et al. Recent development of two-dimensional transition metal dichalcogenides and their applications. *Mater. Today* **20**, 116–130 (2017).
4. Nikonov, D. E. & Young, I. A. Benchmarking of beyond-CMOS exploratory devices for logic integrated circuits. *IEEE J. Explor. Solid-State Comput. Devices Circuits* **1**, 3–11 (2015).
5. Sylvia, S. S., Alam, K. & Lake, R. K. Uniform benchmarking of low-voltage van der Waals FETs. *IEEE J. Explor. Solid-State Comput. Devices Circuits* **2**, 28–35 (2016).
6. Lee, C.-S., Cline, B., Sinha, S., Yeric, G. & Wong, H. S. P. 32-bit processor core at 5-nm technology: analysis of transistor and interconnect impact on VLSI system performance. In *2016 IEEE International Electron Devices Meeting (IEDM)* 28.3.1–28.3.4 (IEEE, 2016).
7. Agarwal, T. et al. Benchmarking of monolithic 3D integrated MX_2 FETs with Si FinFETs. In *2017 IEEE International Electron Devices Meeting (IEDM)* 5.7.1–5.7.4 (IEEE, 2017).
8. Geng, D. & Yang, H. Y. Recent advances in growth of novel 2D materials: beyond graphene and transition metal dichalcogenides. *Adv. Mater.* **30**, 1800865 (2018).
9. Sebastian, A., Pendurthi, R., Choudhury, T. H., Redwing, J. M. & Das, S. Benchmarking monolayer MoS_2 and WS_2 field-effect transistors. *Nat. Commun.* **12**, 693 (2021).
10. Shen, P.-C. et al. Ultralow contact resistance between semimetal and monolayer semiconductors. *Nature* **593**, 211–217 (2021).
11. Li, W. et al. Approaching the quantum limit in two-dimensional semiconductor contacts. *Nature* **613**, 274–279 (2023).
12. English, C. D., Smithe, K. K. H., Xu, R. L. & Pop, E. Approaching ballistic transport in monolayer MoS_2 transistors with self-aligned 10 nm top gates. In *2016 IEEE International Electron Devices Meeting (IEDM)* 5.6.1–5.6.4 (IEEE, 2016).
13. Zhang, Y. et al. A single-crystalline native dielectric for two-dimensional semiconductors with an equivalent oxide thickness below 0.5 nm. *Nat. Electron.* **5**, 643–649 (2022).
14. Li, T. et al. A native oxide high-κ gate dielectric for two-dimensional electronics. *Nat. Electron.* **3**, 473–478 (2020).
15. Schulman, D. S., Arnold, A. J. & Das, S. Contact engineering for 2D materials and devices. *Chem. Soc. Rev.* https://doi.org/10.1039/c7cs00828g (2018).
16. Das, S., Chen, H. Y., Penumatcha, A. V. & Appenzeller, J. High performance multilayer MoS_2 transistors with scandium contacts. *Nano Lett.* **13**, 100–105 (2013).
17. Das, S. and Appenzeller, J. WSe_2 field effect transistors with enhanced ambipolar characteristics. *Appl. Phys. Lett.* **103**, 103501 (2013).
18. Zhang, X. et al. Defect-controlled nucleation and orientation of WSe_2 on hBN: a route to single-crystal epitaxial monolayers. *ACS Nano* https://doi.org/10.1021/acsnano.8b09230 (2019).
19. Zhang, Z., Guo, Y. & Robertson, J. Origin of weaker Fermi level pinning and localized interface states at metal silicide Schottky barriers. *J. Phys. Chem. C* **124**, 19698–19703 (2020).
20. Stolz, S. et al. Layer-dependent Schottky contact at van der Waals interfaces: V-doped WSe_2 on graphene. *npj 2D Mater. Appl.* **6**, 66 (2022).
21. Zhu, G.-J., Xu, Y.-G., Gong, X.-G., Yang, J.-H. & Yakobson, B. I. Dimensionality-inhibited chemical doping in two-dimensional semiconductors: the phosphorene and MoS_2 from charge-correction method. *Nano Lett.* **21**, 6711–6717 (2021).
22. Chowdhury, S., Venkateswaran, P. & Somvanshi, D. A systematic study on the electronic structure of 3*d*, 4*d*, and 5*d* transition metal-doped WSe_2 monolayer. *Superlattices Microstruct.* **148**, 106746 (2020).
23. McClellan, C. J., Yalon, E., Smithe, K. K., Suryavanshi, S. V. & Pop, E. High current density in monolayer MoS_2 doped by AlO_x. *ACS Nano* **15**, 1587–1596 (2021).
24. Tongay, S. et al. Thermally driven crossover from indirect toward direct bandgap in 2D semiconductors: $MoSe_2$ versus MoS_2. *Nano Lett.* **12**, 5576–5580 (2012).
25. Ghosh, S. K. & Somvanshi, D. First-principal insight of the gold-metal interaction to bilayer $MoSe_2$ of AB and AA stacking order. *Solid State Commun.* **342**, 114613 (2022).
26. Bhattacharyya, S. & Singh, A. K. Semiconductor-metal transition in semiconducting bilayer sheets of transition-metal dichalcogenides. *Phys. Rev. B* **86**, 075454 (2012).
27. Gusakova, J. et al. Electronic properties of bulk and monolayer TMDs: theoretical study within DFT framework (GVJ-2e method). *Phys. Status Solidi (a)* **214**, 1700218 (2017).
28. Kuc, A., Zibouche, N. & Heine, T. Influence of quantum confinement on the electronic structure of the transition metal sulfide TS_2. *Phys. Rev. B* **83**, 245213 (2011).
29. Nasr, J. R., Schulman, D. S., Sebastian, A., Horn, M. W. & Das, S. Mobility deception in nanoscale transistors: an untold contact story. *Adv. Mater.* **31**, 1806020 (2019).
30. Chou, A.-S. et al. High-performance monolayer WSe_2 p/n FETs via antimony-platinum modulated contact technology towards 2D CMOS electronics. In *2022 International Electron Devices Meeting (IEDM)* 7.2.1–7.2.4 (IEEE, 2022).
31. Cai, L. et al. Rapid flame synthesis of atomically thin MoO_3 down to monolayer thickness for effective hole doping of WSe_2. *Nano Lett.* **17**, 3854–3861 (2017).
32. Chiang, C.-C., Lan, H.-Y., Pang, C.-S., Appenzeller, J. & Chen, Z. Air-stable P-doping in record high-performance monolayer WSe_2 devices. *IEEE Electron Device Lett.* **43**, 319–322 (2021).
33. Pandey, S. K. et al. Controlled p-type substitutional doping in large-area monolayer WSe_2 crystals grown by chemical vapor deposition. *Nanoscale* **10**, 21374–21385 (2018).
34. Kozhakhmetov, A. et al. Controllable p-type doping of 2D WSe_2 via vanadium substitution. *Adv. Funct. Mater.* **31**, 2105252 (2021).
35. Vu, V. T. et al. One-step synthesis of $NbSe_2$/Nb-doped-WSe_2 metal/doped-semiconductor van der Waals heterostructures for doping controlled ohmic contact. *ACS Nano* **15**, 13031–13040 (2021).

36. Li, X. et al. Isoelectronic tungsten doping in monolayer $MoSe_2$ for carrier type modulation. *Adv. Mater.* **28**, 8240–8247 (2016).
37. Zhong, F. et al. Substitutionally doped $MoSe_2$ for high-performance electronics and optoelectronics. *Small* **17**, 2102855 (2021).
38. Fang, H. et al. High-performance single layered WSe_2 p-FETs with chemically doped contacts. *Nano Lett.* **12**, 3788–3792 (2012).
39. Pang, C. S. et al. Atomically controlled tunable doping in high-performance WSe_2 devices. *Adv. Electron. Mater.* **6**, 1901304 (2020).
40. Yamamoto, M., Nakaharai, S., Ueno, K. & Tsukagoshi, K. Self-limiting oxides on WSe_2 as controlled surface acceptors and low-resistance hole contacts. *Nano Lett.* **16**, 2720–2727 (2016).
41. Yang, S., Lee, G. & Kim, J. Selective p-doping of 2D WSe_2 via UV/ozone treatments and its application in field-effect transistors. *ACS Appl. Mater. Interfaces* **13**, 955–961 (2020).
42. Zhang, T. et al. Universal in situ substitutional doping of transition metal dichalcogenides by liquid-phase precursor-assisted synthesis. *ACS Nano* **14**, 4326–4335 (2020).
43. Pham, Y. T. H. et al. Tunable ferromagnetism and thermally induced spin flip in vanadium-doped tungsten diselenide monolayers at room temperature. *Adv. Mater.* **32**, 2003607 (2020).
44. Chou, A. S. et al. High-performance monolayer WSe_2 p/n FETs via antimony-platinum modulated contact technology towards 2D CMOS electronics. In *2022 International Electron Devices Meeting (IEDM)* 7.2.1–7.2.4 (IEEE, 2022).

Acknowledgements

We thank L. J. Liermann for conducting the ICP-AES analysis, J. M. Anderson for conducting the SEM-EDS analysis on the doped crystals and Y. Zheng for assisting in the oxygen plasma treatment of the fabricated devices. Our sincere gratitude also goes to the Penn State Nanofabrication staff and the cleanroom facility at the Materials Research Institute (MRI), Penn State, where all the device fabrication was carried out. The work was supported by the National Science Foundation (NSF) through a CAREER Award under grant no. ECCS-2042154. Z.S. was supported by ERC-CZ programme (project LL2101) from Ministry of Education Youth and Sports (MEYS) and by the project Advanced Functional Nanorobots (reg. no. CZ.02.1.01/0.0/0.0/15_003/0000444 financed by the ERDF). A.P. was supported by a NASA Space Technology Graduate Research Opportunity grant (no. 80NSSC23K1197). K.J.S. was supported by the Johannes Amos Comenius Programme, European Structural and Investment Funds, project CHEMFELLS VI (no. CZ.02.01.01/00/22_010/0008122).

Author contributions

S.D. conceived the idea and designed the experiments. M.D., D. Sen., N.U.S., H.R., P.V., M.U.K.S. and S.S.R. fabricated and measured the devices. Y.S., Z.Z., Y.H. and Y.Y. obtained and analysed the high-resolution cross-sectional TEM data. D.E.S performed the c-axis high-resolution TEM on the doped $MoSe_2$ crystals. A.S., Z.Y. and M.T. grew the Nb-doped $MoSe_2$. K.J.S., K.M. and Z.S. grew the Nb-, V- and Ta-doped $MoSe_2$ and WSe_2 crystals. A.P. helped with the AFM measurements. S.G. and D. Somvanshi. performed the DFT simulations. All authors contributed to the preparation of the paper.

Competing interests

The authors declare no competing interests.

Additional information

Extended data is available for this paper at https://doi.org/10.1038/s41928-024-01265-2.

Supplementary information The online version contains supplementary material available at https://doi.org/10.1038/s41928-024-01265-2.

Correspondence and requests for materials should be addressed to Saptarshi Das.

Peer review information *Nature Electronics* thanks Ruge Quhe and the other, anonymous, reviewer(s) for their contribution to the peer review of this work.

Reprints and permissions information is available at www.nature.com/reprints.

Publisher's note Springer Nature remains neutral with regard to jurisdictional claims in published maps and institutional affiliations.

[1]Engineering Science and Mechanics, Penn State University, University Park, PA, USA. [2]Department of Physics, Penn State University, University Park, PA, USA. [3]Department of Inorganic Chemistry, University of Chemistry and Technology Prague, Prague, Czech Republic. [4]Department of Physics, Harcourt Butler Technical University, Kanpur, India. [5]Materials Science and Engineering, Penn State University, University Park, PA, USA. [6]Nuclear Engineering, Penn State University, University Park, PA, USA. [7]Electrical Engineering, Penn State University, University Park, PA, USA. [8]These authors contributed equally: Mayukh Das, Dipanjan Sen. ✉e-mail: sud70@psu.edu

https://doi.org/10.1038/s41928-024-01265-2

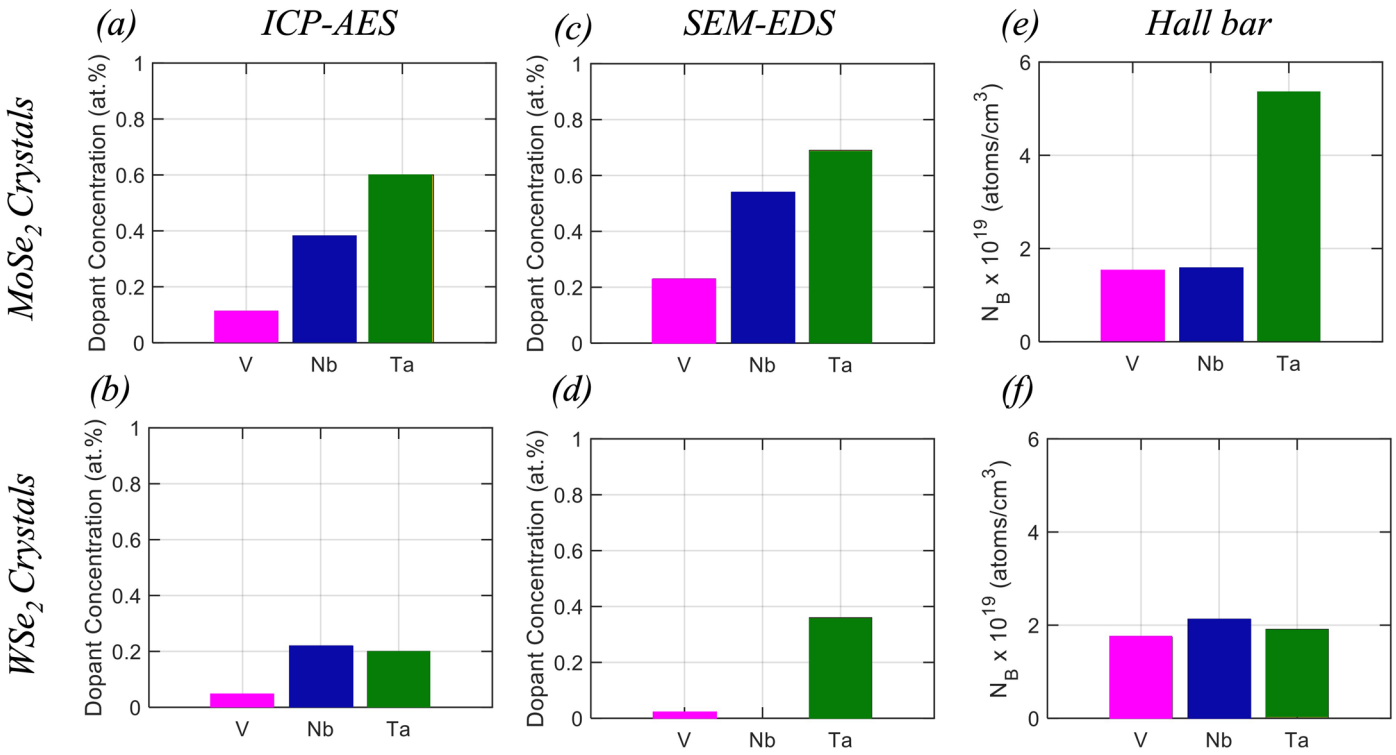

Extended Data Fig. 1 | Dopant concentration in V-, Nb-, and Ta-doped $MoSe_2$ and WSe_2 crystals. Bar plots showing the dopant concentrations for V, Nb, and Ta, determined using inductively coupled plasma atomic emission spectroscopy (ICP-AES) for **a**) $MoSe_2$ and **b**) WSe_2. Dopant concentrations for V, Nb, and Ta, extracted using scanning electron microscopy-electron dispersive X-ray spectroscopy (SEM-EDS) for **c**) $MoSe_2$ and **d**) WSe_2. Bulk carrier concentrations (N_B) at room temperature, obtained from Hall measurements for **e**) $MoSe_2$ and **f**) WSe_2 doped with V, Nb, and Ta.

https://doi.org/10.1038/s41928-024-01265-2

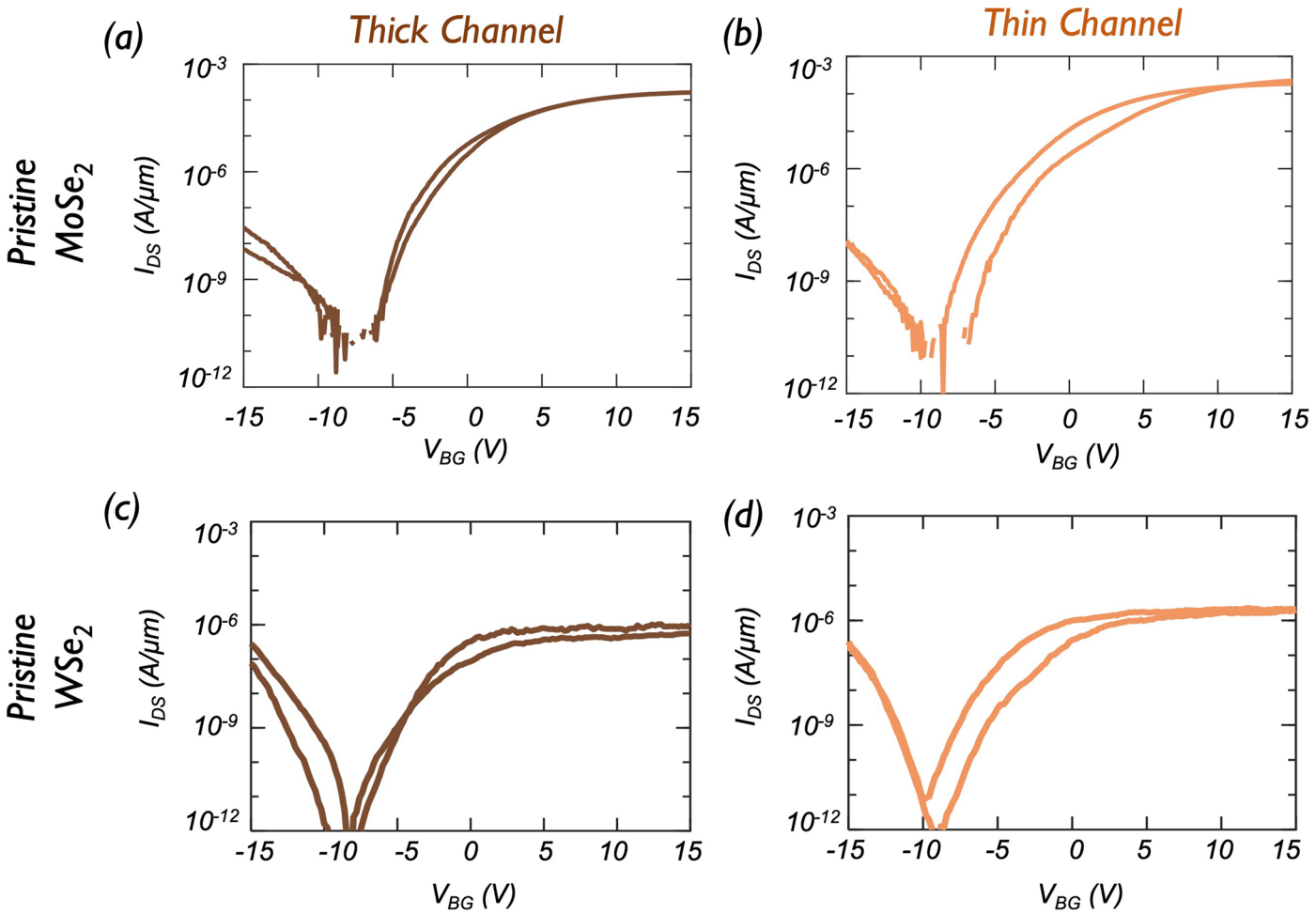

Extended Data Fig. 2 | Electrical characterization of pristine $MoSe_2$ and WSe_2 FETs. Transfer characteristics for **a**) two thick (~4–6 monolayers) and **b**) two thin (~1–3 monolayers) $MoSe_2$ FETs. Transfer characteristics for **c**) two thick (~4–6 monolayers) and **d**) two thin (~1–3 monolayers) WSe_2 FETs at V_{DS} = 1 V.

https://doi.org/10.1038/s41928-024-01265-2

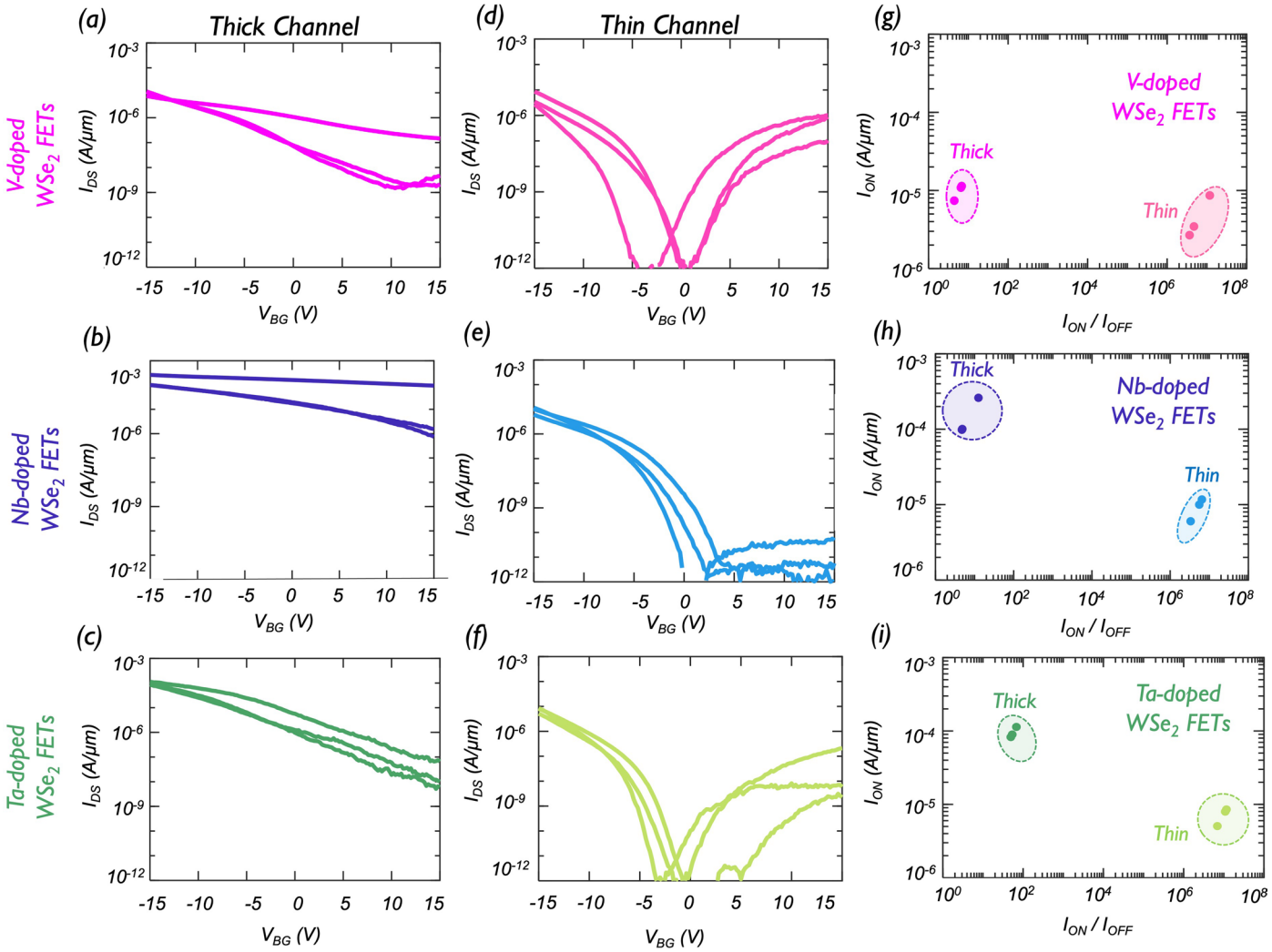

Extended Data Fig. 3 | Substitutionally doped p-type WSe_2 FETs. Transfer characteristics, that is, source-to-drain current (I_{DS}) as a function of the back-gate voltage (V_{BG}) for a constant source-to-drain bias of V_{DS} = 1 V for **a**) V-, **b**) Nb-, and **c**) Ta-doped WSe_2 FETs with thick (~4–6 monolayers) channels. These FETs show high on-state current (I_{ON}) (except for the case of V-doped WSe_2) and poor electrostatic gate control (low I_{ON}/I_{OFF}) confirming degenerate p-type doping. In contrast, transfer characteristics for **d**) V-, **e**) Nb-, and **f**) Ta-doped WSe_2 FETs with thin (~1–3 monolayers) channels retained high I_{ON}/I_{OFF} more than 10^5. However, I_{ON} values were significantly lower. Corresponding scatter plots with I_{ON} measured at V_{BG} = −15 V and I_{ON}/I_{OFF} as the two axes for **g**) V-, **h**) Nb-, and **i**) Ta-doped FETs with thick and thin WSe_2 channels. All FETs have a channel length (L_{CH}) of 500 nm.

https://doi.org/10.1038/s41928-024-01265-2

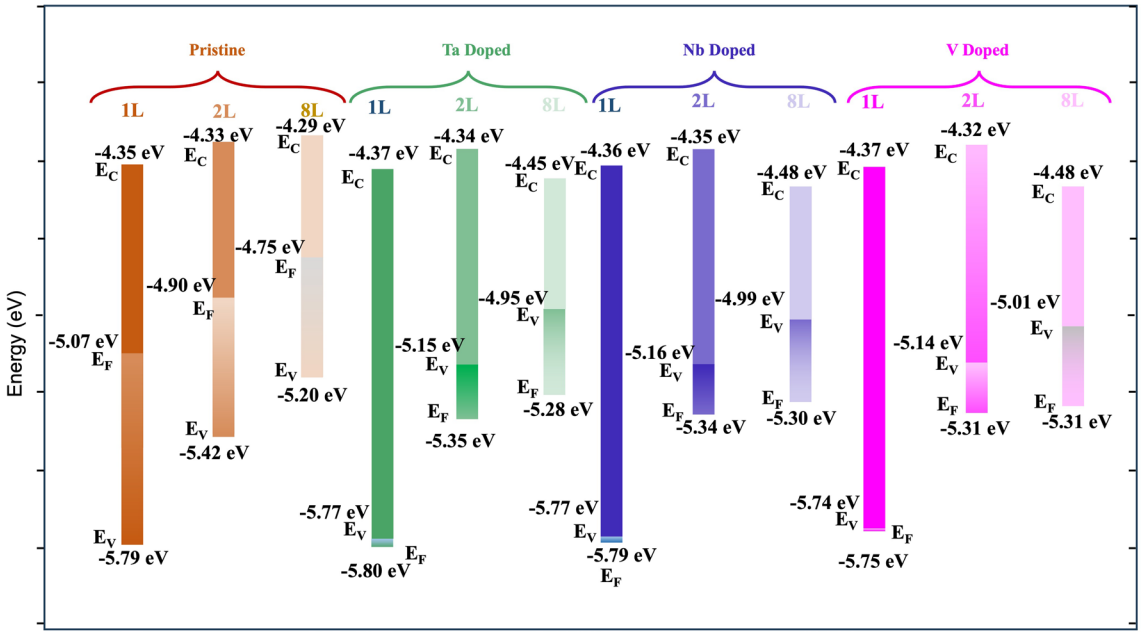

Extended Data Fig. 4 | Band alignment of pristine and doped1L, 2L and 8L-$MoSe_2$. In this observation, it is evident that the introduction of V, Nb, and Ta doping results in a reduction of the band gap, and there is also a notable shift of the Fermi level below the valence band.

https://doi.org/10.1038/s41928-024-01265-2

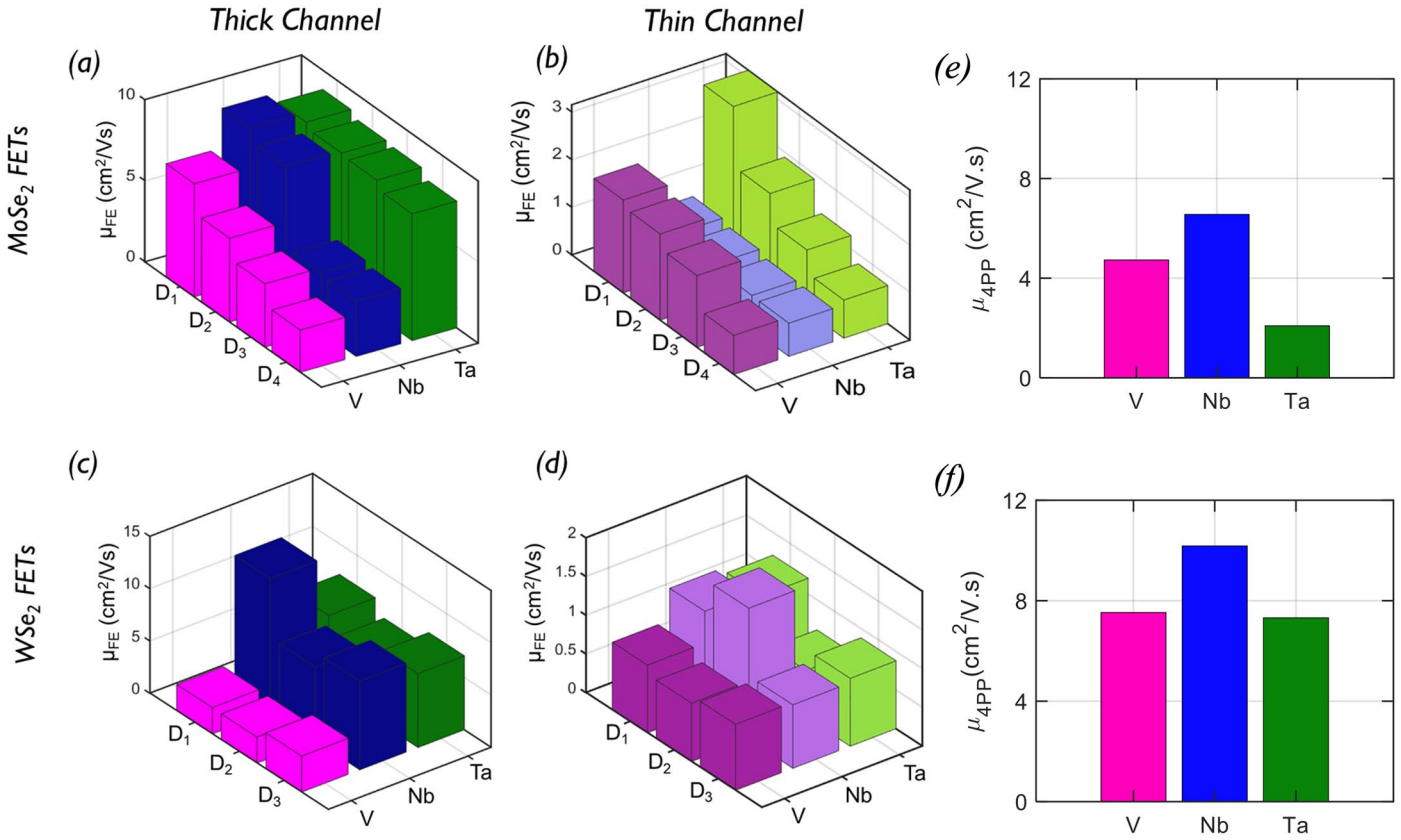

Extended Data Fig. 5 | Field effect mobility (μ_{FE}) and 4-point probe mobility (μ_{4PP}) for $MoSe_2$ and WSe_2 FETs. Hole field-effect mobility (μ_{FE}), extracted from peak transconductance for **a**) thick channel and **b**) thin channel FETs based on V-, Nb-, and Ta-doped $MoSe_2$ and for **c**) thick channel and **d**) thin channel FETs based on V-, Nb-, and Ta-doped WSe_2. Bar plots showing the 4-point probe mobility (μ_{4PP}) extracted from Hall measurement for holes for **e**) $MoSe_2$ and **f**) WSe_2 specimens with dopants V, Nb, and Ta.

https://doi.org/10.1038/s41928-024-01265-2

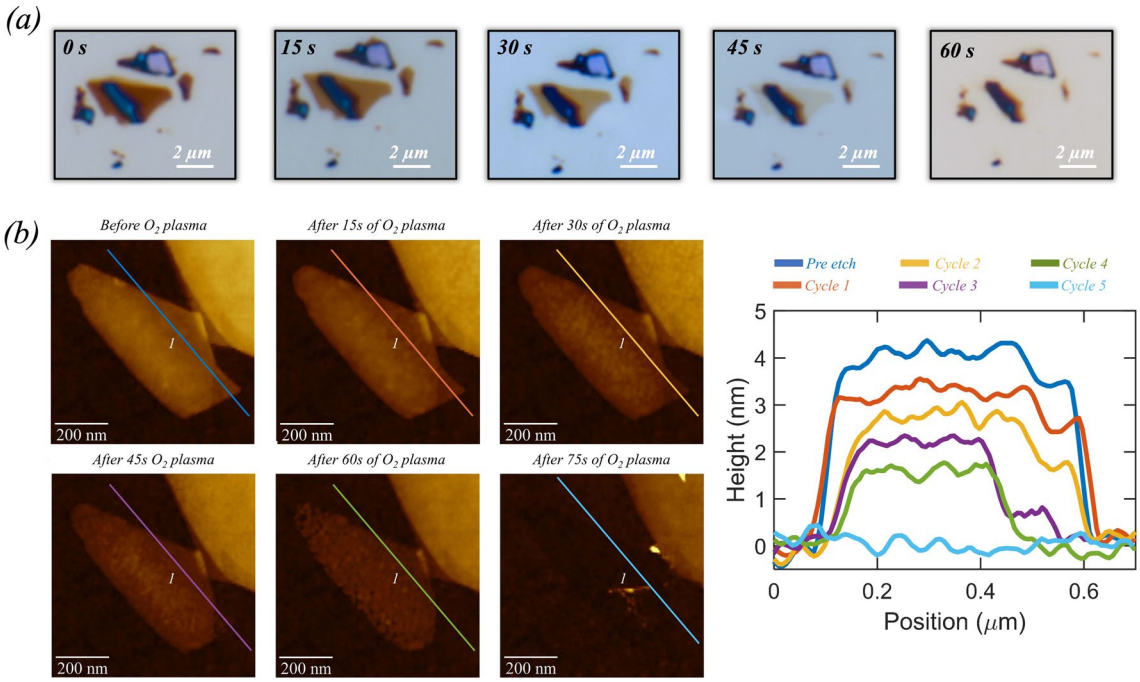

Extended Data Fig. 6 | Layer by layer thinning of multilayer $MoSe_2$ flake. **a**) Optical images of $MoSe_2$ flakes taken before and after successive treatment with mild oxygen plasma followed by DI water rinse to remove the top-layer of MoO_x. The layer-by-layer thinning is evident from the contrast of the flakes that transitions from a deep brown hue to a lighter shade of brown. **b**) AFM images of the evolution of layer-by-layer thinning of $MoSe_2$ flakes subjected to O_2 plasma. Each plasma step is followed by a DI water dip before subsequent AFM measurements. The height profile of the flake along line 1 is also depicted and reveals a reduction of about 0.8 nm after each plasma step suggesting the removal of a single layer of $MoSe_2$ flake.

https://doi.org/10.1038/s41928-024-01265-2

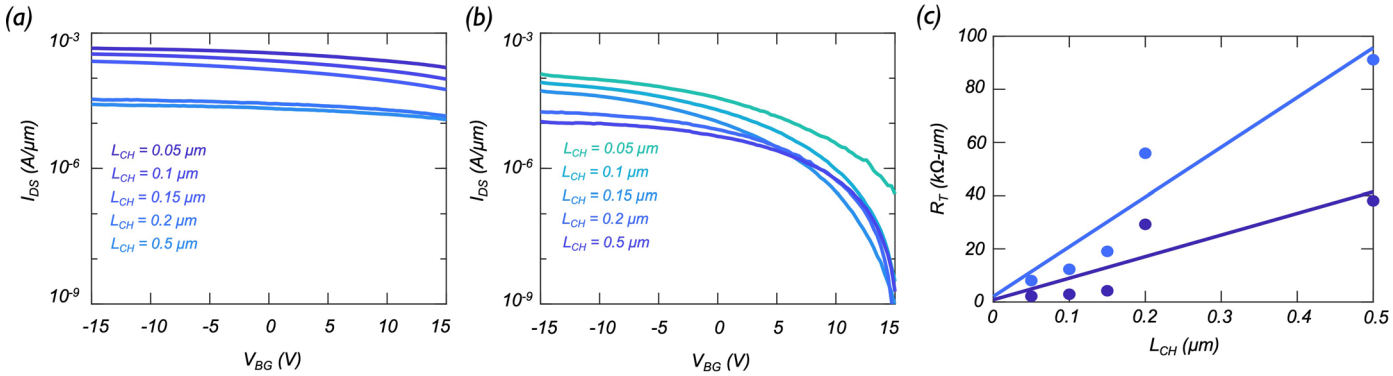

Extended Data Fig. 7 | As-fabricated and post-processed Nb-doped $MoSe_2$ FETs. Transfer characteristics of **a**) as-fabricated and **b**) post-processed Nb-doped $MoSe_2$ FETs with L_{CH} = 50 nm, 100 nm, 150 nm, 200 nm, and 500 nm. Three successive rounds of oxygen plasma treatment, followed by immersion in DI water, were carried out to reduce the thickness of the channel between the contacts while keeping the channel thicker underneath the contacts. **c**) Corresponding total resistance R_T (normalized by width) measured at V_{BG} = −15 V versus L_{CH} for as-fabricated and post-processed Nb-doped $MoSe_2$ FETs at V_{DS} = 1 V.

https://doi.org/10.1038/s41928-024-01265-2

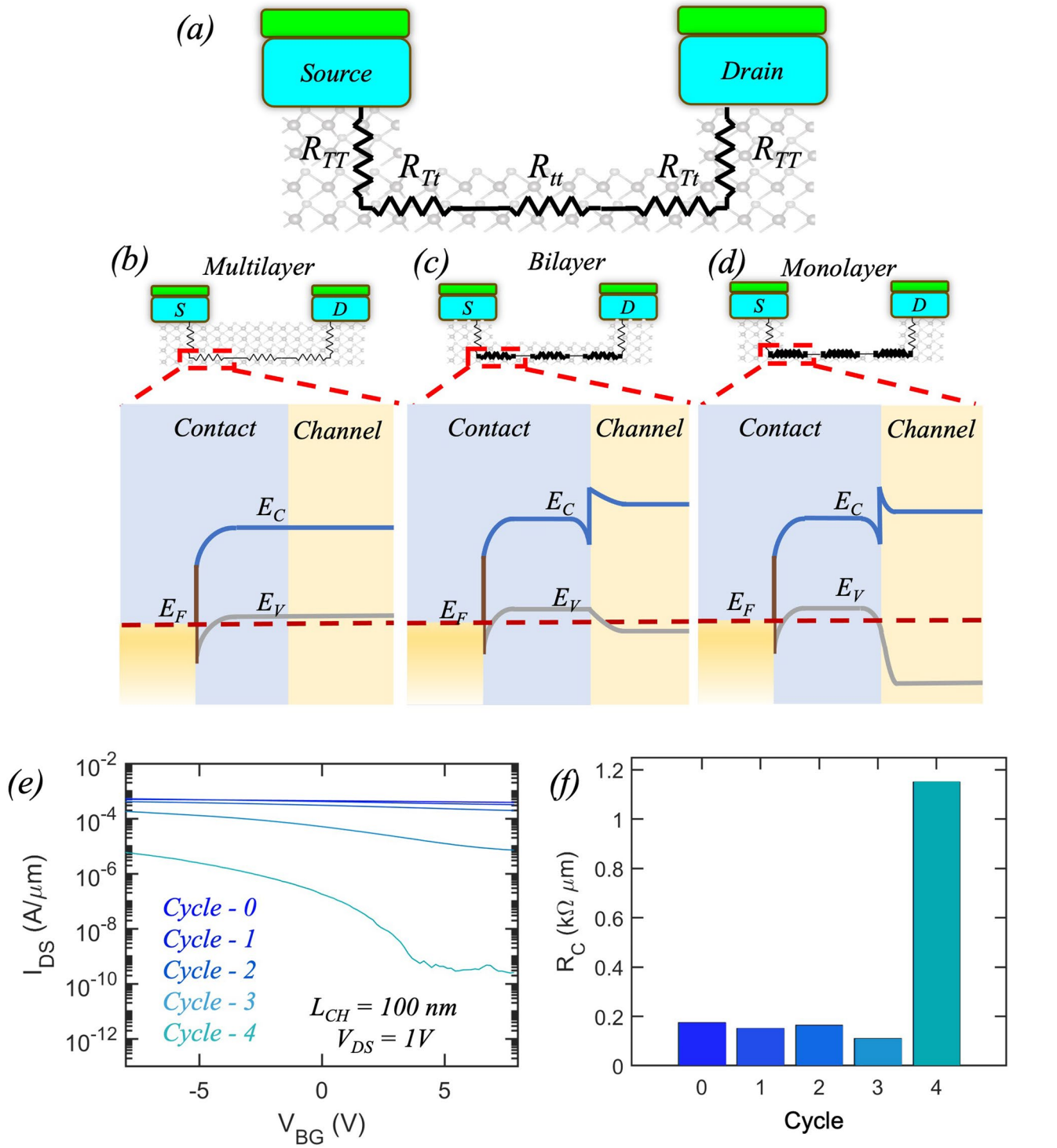

Extended Data Fig. 8 | Resistor network for carrier transport in our proposed 2D FET. (**a**) A resistor network with essential resistance components associated with carrier transport in our proposed 2D FET structure. Schematic and corresponding band-diagrams for $MoSe_2$ based 2D FETs with thick channels underneath the contacts and (**b**) multilayer, (**c**) bilayer and (**d**) monolayer channels between the contacts. The bandgap mismatch between thick and thin MoSe2 layers give rise to an additional energy barrier at the interface between the thinner channel and thicker contact regions. This energy barrier remains relatively small for channels over 2 layers, as the $MoSe_2$ bandgap stays nearly constant. However, the barrier height can increase markedly when the channel becomes monolayer, due to the transition from indirect to direct bandgap between bi-layer and monolayer. This alteration can lead to a considerable increase in R_C. (**e**) Transfer characteristics of a multilayer Nb-doped $MoSe_2$ FET after each etch cycle, and (**f**) corresponding bar plot of the R_C values obtained from TLM measurements.

https://doi.org/10.1038/s41928-024-01265-2

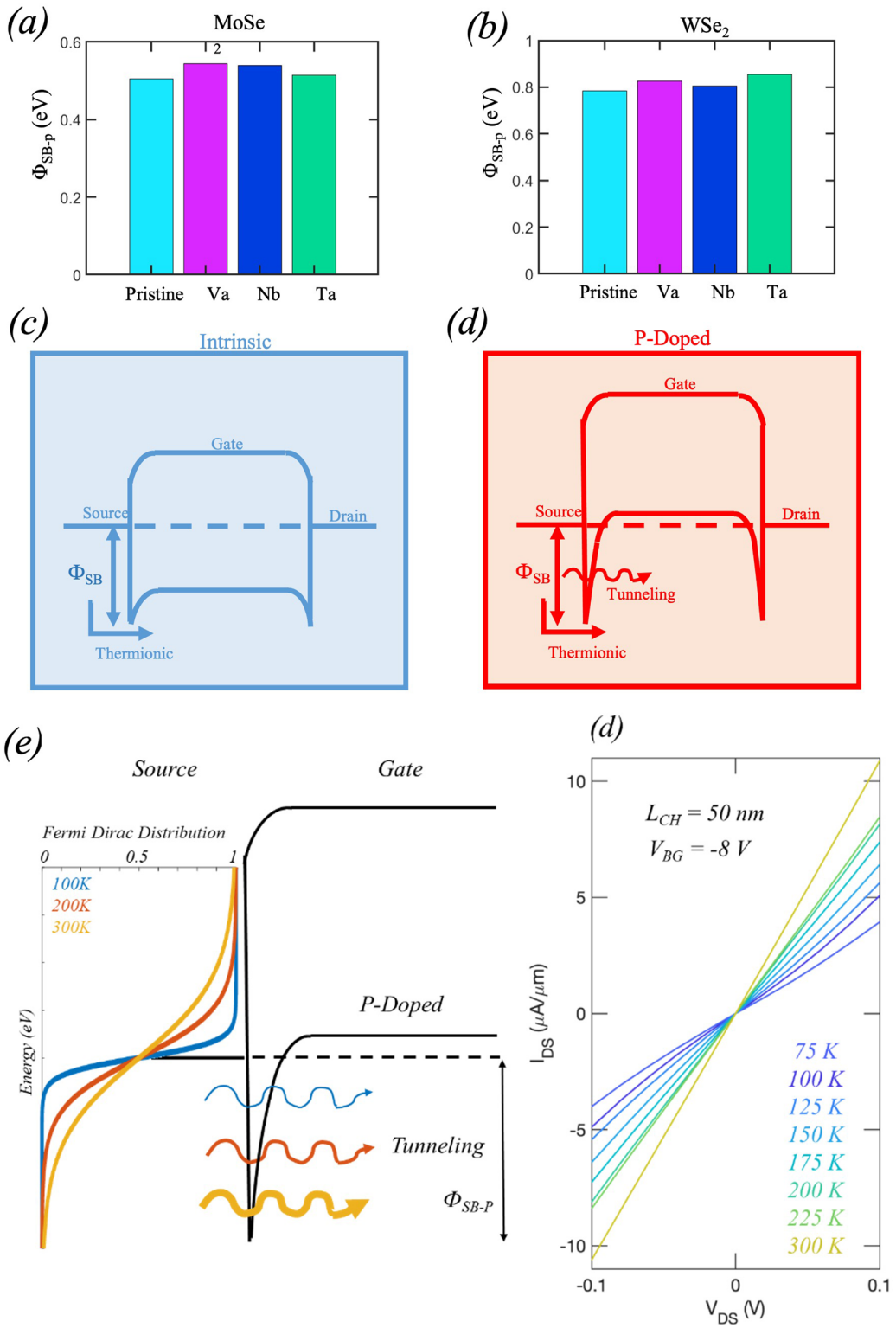

Extended Data Fig. 9 | Extraction of Schottky barrier ($\phi_{SB\text{-}P}$) heights for doped $MoSe_2$ and WSe_2 FETs and temperature dependence of output characteristics for Nb-doped $MoSe_2$ DGFETs. ϕ_{SB-P} values were obtained for pristine, V-, Nb-, and Ta-doped **a**) $MoSe_2$ and **b**) WSe_2 FETs. **c-d**) Schematic of band diagrams for intrinsic and heavily p-type doped semiconductors in contact with a metal. **e**) Band diagram portraying the broadening of the Fermi-Dirac tail with increasing temperature, providing additional holes for tunnelling through the narrower region of the Schottky barrier. The enhanced tunnelling of holes results in a Ohmic like characteristics at higher temperatures. Output characteristics measured at a constant V_{BG} of −8 V as the temperature is increased from 75 K to 300 K. The output characteristics transitioned from mostly Schottky type to nearly Ohmic-like.

https://doi.org/10.1038/s41928-024-01265-2

Extended Data Table 1 | Benchmarking table showing the advances demonstrated in this work over previous attempts at achieving high performance p-type 2D FETs

TMDC	Growth	TMDC thickness (nm)	Dopant	Carrier Concentration , n_s (cm^{-2})	Channel Length, $L_{CH}(\mu m)$	On-state current at $\lvert V_{DS}\rvert \sim 1\ V$, I_{ON} ($\mu A/\mu m$)	Field-effect mobility, μ (cm^2/Vs)	ON-OFF Ratio, I_{ON}/I_{OFF}	Contact Resistance , R_C ($K\Omega.\mu m$	Subthreshold Slope, SS (mV/dec)	Ref.
WSe_2	CVT	0.7	NO_2	2.2 x 10^{12}	9.4	10	250	> 10^6	--	60	[38]
WSe_2	CVT	4	MoO_3	5 x 10^{13}	0.4	100	--	10	0.8	--	[31]
WSe_2	CVD	3.5	WO_3	8.3 x 10^{12}	0.065	320	--	10	0.528	--	[39]
WSe_2	CVT	1.4	WO_3	2.6 x 10^{12}	1	10	57	~ 10	1.1	--	[40]
WSe_2	CVD	0.7	NO_x	--	0.065	300	35	2 x 10^6	0.95	222	[32]
WSe_2	CVT	5.1	WO_3	--	5	7 ($V_{DS} = 2\ V$)	72.9	2.46 × 10^8	109.6	~ 1200	[41]
WSe_2	CVD	0.7	MoO_x	~ 1 x 10^{13}	0.1	151	--	--	0.75	--	[42]
WSe_2	CVD	0.7	Nb	9 x 10^{11}	3	10 ($V_{DS} = 0.1\ V$)	116	10^6	0.55	> 3000	[33]
WSe_2	CVD	0.7	V	--	1	5	--	10^6	--	> 300	[34]
WSe_2	CVD	0.7	Nb	1.4 x 10^{12}	12	17.9	27.24	2.2 × 10^7	2.46	--	[35]
$MoSe_2$	CVD	0.7	W	4 x 10^{11}	> 10	10 ($V_{DS} = 2\ V$)	1.6	10^6	--	--	[36]
$MoSe_2$	CVT	6.2	Ta	8.42 x 10^{11}	> 15	3 ($V_{DS} = 0.5\ V$)	2.65	10^7	--	--	[37]
$MoSe_2$	CVT	~ 4.2	Ta	4 x 10^{13}	0.1	527	7	15	0.4	--	This work
$MoSe_2$	CVT	~ 4.2	Ta	2 x 10^{13}	0.1	100	7	~ 10^4	5	3000	This work
$MoSe_2$	CVT	~ 6	Ta	--	0.05	960	--	~ 1.1	0.125	--	This work
$MoSe_2$	CVT	~ 4.2	Nb	2 x 10^{13}	0.1	85	8.5	4 x 10^4	2	1100	This work
$MoSe_2$	CVT	~ 2.8	Nb	3 x 10^{13}	0.05	212	--	~ 10^4	--	3000	This work
$MoSe_2$	CVT	~ 6	Nb	--	0.05	1800	--	~ 1.1	0.095	--	This work